Heterochronous laminar maturation in the human prefrontal cortex

Valerie J. Sydnor[1,2*], Daniel Petrie[1,2], Shane D. McKeon[1-3], Alyssa Famalette[1], Will Foran[1], Finnegan J. Calabro[1,3], Beatriz Luna[1-3*]

* correspondence to: sydnorvj@upmc.edu and lunab@upmc.edu

Affiliations

1. Department of Psychiatry, University of Pittsburgh Medical Center, University of Pittsburgh, Pittsburgh, PA, USA;
2. The Center for the Neural Basis of Cognition, University of Pittsburgh and Carnegie Mellon University, Pittsburgh, PA, USA;
3. Department of Bioengineering, University of Pittsburgh, Pittsburgh, PA, USA.

Abstract

The human prefrontal cortex (PFC) exhibits markedly protracted developmental plasticity, yet whether reductions in plasticity occur synchronously across prefrontal cortical layers is unclear. Animal studies have shown that intracortical myelin consolidates neural circuits to close periods of plasticity. Here, we use quantitative myelin imaging collected from youth (ages 10-32 years) at ultra-high field (7T) to investigate whether deep and superficial PFC layers exhibit different timeframes of plasticity. We find that myelin matures along a deep-to-superficial axis in the PFC; this axis of maturational timing is expressed to a different extent in cytoarchitecturally distinct regions along the frontal cortical hierarchy. By integrating myelin mapping with electroencephalogram and cognitive phenotyping, we provide evidence that deep and superficial prefrontal myelin dissociably impact timescales of neural activity, task learning rates, and cognitive processing speed. Heterochronous maturation across deep and superficial layers is an underrecognized mechanism through which association cortex balances cognitively-relevant increases in circuit stability and efficiency with extended neuroplasticity.

Introduction

The human prefrontal cortex (PFC) is an evolutionarily-expanded core of association cortex[1–3] that supports advanced cognitive processing and exhibits remarkably protracted development during childhood and adolescence[3–7]. The PFC's capacity to develop over decades suggests that it balances developmental increases in circuit stability necessary for reliable cognitive functioning with continued circuit malleability fundamental to experience-dependent refinement. In this study, we investigate the hypothesis that this balance is achieved through the heterochronous maturation of biological regulators of plasticity across layers of the PFC. Far from being a uniform entity, the PFC is a mosaic of both functionally diverse cortical regions and distinct cortical layers that exhibit substantial developmental variability[3,5,7]. Prior work investigating this variability has revealed that reductions in plasticity progress hierarchically across frontal regions[5,8–11], facilitated by asynchronous increases in intracortical myelin, a primary regulator of neuronal plasticity[5,12–14]. However, how plasticity temporally unfolds across prefrontal cortical layers—which differ in their evolutionary histories, connectivity targets, neurobiological features, and functional roles—is a fundamental unknown in our understanding of association cortex developmental chronology. Here, we harness ultra-high field quantitative imaging of intracortical myelin collected *in vivo* and longitudinally to characterize timescales of plasticity across deep and superficial layers of the developing frontal cortex and relate PFC myelination to neurocognitive specialization.

The prefrontal cortical ribbon has a classic laminar architecture defined by the presence of up to six cortical layers. Although layers are not equivalent across frontal regions[3,15], they conform to a canonical circuit architecture with stereotypical input connections and output projections. Layers 1 and 4 are non-pyramidal "input" layers that receive substantial input from the thalamus and other cortical regions. Layers 5 and 6 are pyramidal layers in deep cortex that serve as the main cortical "output" layers. These layers contain pyramidal neurons that predominantly project to the subcortex, including to the thalamus, striatum, brainstem, and spinal cord, with a smaller proportion sending feed-back cortical projections[16]. Layers 2 and 3 are pyramidal layers in superficial cortex that are the main source of local and long-range cortico-cortical connections, especially feed-forward projections[16]. Layers 2/3 are proportionally thicker in the PFC of primates than in other mammalian species[17] and have extensive local recurrent excitatory connections[16] with high integrative capacity and coding dimensionality[18]. Layers 2/3 are thus considered the main "computation" layers of the PFC[19,20]. Despite these marked differences between cortical layers, it is not clear whether they exhibit unique trajectories of plasticity that influence structural consolidation versus continued adaptation within the PFC.

One of the primary biological regulators of cortical developmental plasticity is the growth of intracortical myelin[21–23]. Myelin forms in the cortex around the axons of both pyramidal neurons[24] and parvalbumin (PV) inhibitory interneurons[25,26]: the two main neural substrates for remodeling during periods of heightened developmental plasticity[27,28]. Once myelin is formed, myelin-associated inhibitors (Nogo, MAG, OMgp)[29] interact with receptors expressed on neurons to inhibit neurite outgrowth[30], spine turnover[21,31], and synaptic plasticity[32]. As a result, myelin formation serves to consolidate the physical wiring of circuitry and close developmental windows of neuronal plasticity. Notably, although myelin formation restricts structural plasticity of neurons, myelin itself remains relatively plastic throughout life[33–36]. Indeed, in animal models, activity-dependent myelin sheath formation and restructuring continues into adulthood and is instrumental for learning and long-term memory[34,37–40]. Intracortical myelin thus serves as both a key regulator of developmental plasticity and a structural foundation for lifelong cognitive refinement.

Prior elegant studies using *in vivo* imaging to study the development of intracortical myelin have found that deep-to-mid depths of the prefrontal cortical ribbon myelinate more than superficial depths during the adolescent period[11,41–43]. Post-mortem studies of human and non-human primates have furthermore shown that as compared to pyramidal neurons in layer 5, neurons in layer 3 of the adolescent PFC show more pronounced pruning of dendritic spines[6] and slower accumulation of

proteins associated with stable dendritic morphology[10]. These data convergently suggest that superficial prefrontal layers may exhibit more protracted plasticity than deep layers; however, direct *in vivo* evidence for temporal variability in the closure of plasticity across deep and superficial PFC is lacking. This gap precludes an understanding of whether asynchronous laminar maturation allows superficial and deep circuits to differentially contribute to the PFC's extended malleability and the maturation of higher-order cognitive capacities. This gap exists, in part, given that conventional MRI field strengths and contrast-based acquisitions are limited in their capacity to study refinements in plasticity regulators across varying depths of the cortex with adequate sensitivity and specificity. In this study, we overcome these limitations by combining 7 Tesla (7T) MRI, quantitative neuroimaging, and intracortical depth profiling to chart the temporal maturation of myelin throughout the frontal cortical ribbon. Unlike contrast-based approaches, quantitative imaging techniques measure the biochemical composition of tissue using calibrated measures of tissue properties (e.g., proton relaxation times) expressed in physical units. Here, we specifically employ quantitative R1, a histologically-validated, myelin-sensitive imaging measure[44–47] that increases with greater myelin density and has excellent scan-rescan reliability at 7T[48].

We hypothesized that developmental change in prefrontal R1 would follow a deep-to-superficial maturational sequence, providing evidence for earlier consolidation of layer 5/6 projections to subcortex and hierarchically lower regions together with protracted plasticity in layer 2/3 cortico-cortical connections. Furthermore, given evidence that myelination progresses hierarchically across cortical regions[5,12–14], we tested whether variation in R1 development across intracortical depths is differentially expressed across the frontal cortical hierarchy. Finally—leveraging electroencephalogram (EEG) and cognitive assessments collected from the same participants—we studied the impact of superficial and deep cortex myelin on the maturation of circuit electrophysiology and PFC-dependent cognitive processes. The formation of myelin around excitatory pyramidal cells and inhibitory PV interneurons supports high frequency interactions between excitatory (E) and inhibitory (I) firing[49] and increases the speed and fidelity of ongoing neural activity[50,51]. We therefore hypothesized that R1 would correspond to EEG indices of E/I balance and the timescale of activity as well as cognitive measures of learning rate and processing speed. Specifically, we predicted that the protracted formation of myelin in superficial layers would facilitate continual improvements in learning[36,37] whereas earlier myelin maturation in deep layers would support adolescent enhancements in processing speed—leading to depth-specific associations between R1 and cognitive subprocesses. Altogether, we provide evidence for heterochronous myelin maturation across deep and superficial portions of the PFC that allows higher-order association cortex to couple cognitively-relevant increases in circuit stability and efficiency with extended neuroplasticity.

Results

We studied spatiotemporal variability in the maturation of myelin throughout the frontal cortical ribbon in an accelerated longitudinal sample of 140 individuals ages 10-32 years old with 1-3 imaging timepoints each. Myelin was measured with quantitative R1 data (the longitudinal relaxation rate in sec^{-1}) collected at ultra-high field. To characterize laminar variability in myelin density, we used cortical profiling[11,41,43] to quantify R1 at a range of intracortical depths between pial and white matter boundaries. Specifically, we mapped volumetric R1 data to individual-specific cortical surfaces at 7 intracortical depths that were virtually free of partial volume effects (**Supplementary Fig. 1.1**). These 7 depths ranged approximately from the bottom of layer 2 (depth 1; 20% of cortical depth) to above mid-layer 6 (depth 7; 80% of cortical depth)[19,43] (**Fig. 1A**; see Methods). To chart maturational changes in R1 in a depth sensitive manner, we fit depth-specific generalized additive mixed models (GAMMs) in frontal lobe regions. We additionally used GAMMs to study relationships between cortical R1 and individual differences in cortical dynamics and cognitive abilities.

Quantitative imaging of cortical myeloarchitecture in youth

Prior to using R1 to study prefrontal myelin development, we aimed to validate that it captured the expected distribution of myelin across cortical regions and depths in our 7T sample. We first averaged R1 across depths in each region (**Fig. 1B**) and surveyed whether regional differences in this measure aligned with anatomical, transcriptomic, and imaging readouts of variation in cortical myelin density. R1 strongly decreased across the cortex's sensorimotor-association (S-A) axis (r = -0.63, $p_{SA\text{-}null}$, < 0.001; **Fig. 1C**), in line with prior findings that cortical myelin levels are highest in sensory and motor cortices and gradually decline along the cortical hierarchy[3,11,12,52,53]. Across-cortex R1 also positively correlated with myelin basic protein gene expression (r = 0.53, $p_{SA\text{-}null}$ = 0.015; **Fig. 1D**) and the myelin water fraction derived from quantitative T2 relaxation imaging (r = 0.64, $p_{SA\text{-}null}$ < 0.001; **Fig. 1E**).

We next extended our validation of R1 to intracortical depths within the frontal lobe; depth-wise R1 values paralleled those reported in prior myelin mapping literature[47]. Cross-species studies have shown that cortical myelin levels increase between cortical layers 2 and 6[11,22,47,52,53]. Qualitative and quantitative analyses substantiated that in our sample, R1 progressively increased from superficial (depth 1) to deep (depth 7) cortex both within (**Fig. 1F**) and beyond (**Supplementary Fig. 1.2**) the frontal lobe, with subtle differences in the regional patterning of R1 observed across intracortical depths (**Fig. 1G**). Moreover, in agreement with prior histological studies[11,52,53], the rate of depth-dependent increases in R1 varied across cortical regions with different degrees of laminar differentiation (**Fig. 1H**). These findings confirm that R1 captures key features of cortical myeloarchitecture organization both across cortical regions and within the cortical ribbon, supporting its utility for studying myelin maturational dynamics *in vivo*.

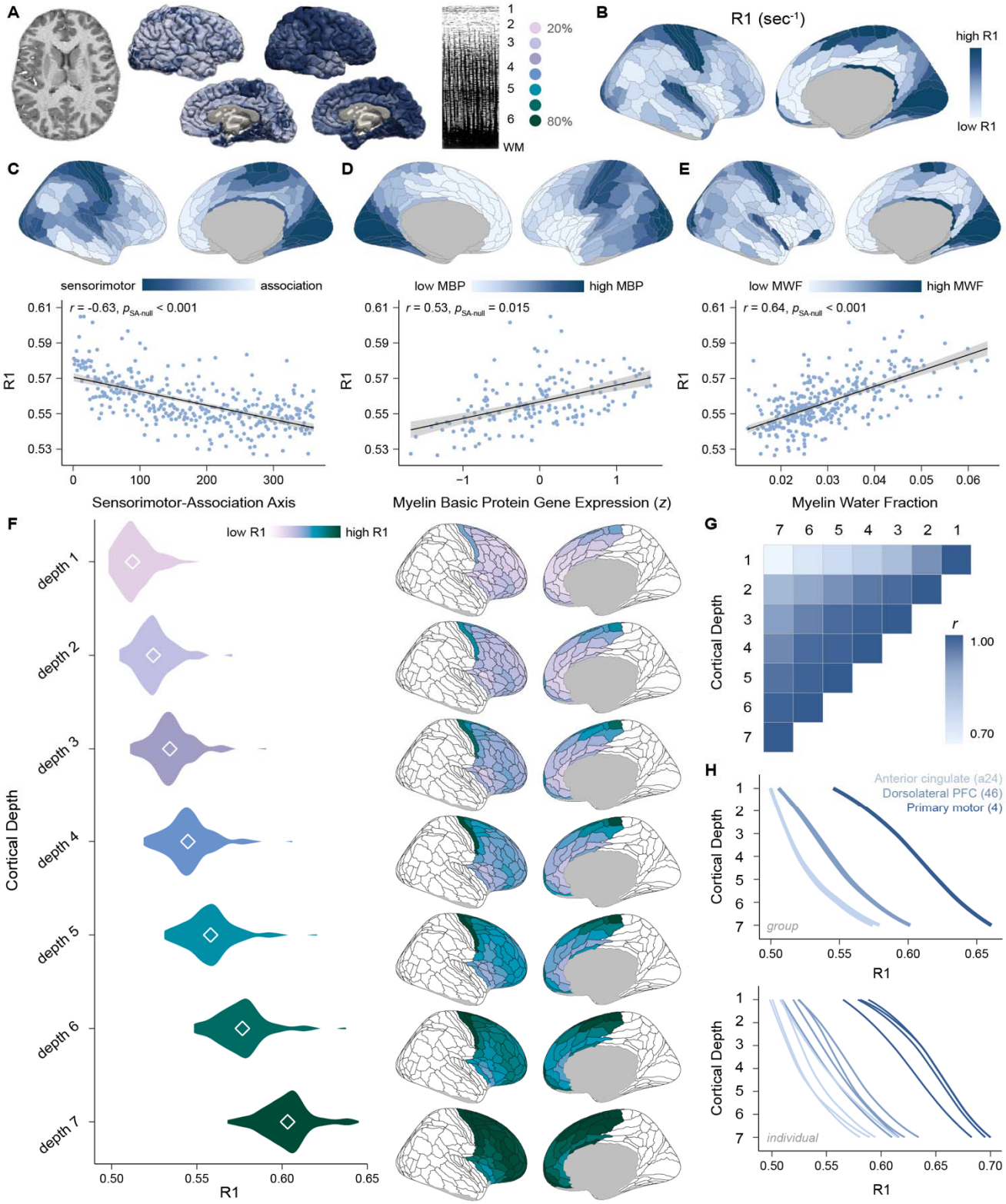

Figure 1. R1 captures myeloarchitectural variation throughout the youth cortex. A) A volumetric R1 map from a representative individual is shown along with projections of R1 to that individual's cortical surface at superficial (left) and deep (right) depths. To provide intuition into the sampling of R1 at 7 intracortical depths, a histochemical myelin stain of prefrontal area 44 is included, along with the labeling of cortical layers 1-6 and

white matter (WM). The estimated locations of the 7 cortical depths under study, which range from 20% to 80% of total cortical thickness, are indicated. The myelin stain is reproduced from Palomero-Gallagher and Zilles, 2019[54]. B) A map of regional average R1 in the 7T youth sample. R1 is a quantitative MRI measure with units of sec^{-1}. C) R1 progressively decreased along the sensorimotor-association axis (cortical map from Sydnor et al.)[3] demonstrating hierarchical variation in this myelin-sensitive measure. D) R1 positively correlated with myelin basic protein (MBP) gene expression (cortical map from Wagstly et al.[55]), demonstrating alignment between R1 and a transcriptomic readout of myelin level. E) Regional differences in R1 were coupled to differences in the myelin water fraction (MWF; cortical map from Liu et al.[56]), confirming spatial correspondence between R1 and an independent myelin mapping technique. F) R1 increases in the frontal lobe with increasing intracortical depth. R1 is shown in frontal regions at each intracortical depth (right) along with corresponding depth-specific violin plots (left). The violin plots summarize the distribution of regional R1 at each depth; white diamonds represent average frontal R1 by depth. G) A Pearson's correlation matrix comparing frontal lobe R1 between pairs of cortical depths reveals that there is high congruence but not equivalence in the regional distribution of R1 at each depth. H) Depth-dependent profiles of R1 differ between three laminarly distinct regions, including the primary motor cortex (area 4), the dorsolateral prefrontal cortex (area 46), and the anterior cingulate (area a24). Regional differences in depth-wise R1 profiles were observable both in group-averaged data (top) and data from individual participants (bottom; three participants shown). Left and right hemisphere depth profiles are plotted separately for each region.

Frontal myelin matures heterochronously across cortical depths

A primary goal of this work was to test the hypothesis that superficial and deep layers of the human PFC exhibit different maturational timeframes. To initially assess this hypothesis, we averaged R1 across the frontal lobe within each of the 7 intracortical depths and fit depth-specific GAMMs, thereby modeling R1 developmental trajectories at different locations in the frontal cortical ribbon. R1 significantly increased with age in all 7 cortical depths ($p_{FDR} < 0.001$ in all 7 models). However, developmental splines showed variability in the degree of increase and the shape of age-related curves across depths (**Fig. 2A; Supplementary Fig. 2.1**). In particular, R1 exhibited shallower and more continuous increases in the most superficial depths. With increasing distance into the cortex, R1 showed larger age-related increases that slowed over time, resulting in trajectories that plateaued in young adulthood. An age-by-depth interaction that tested whether age splines were significantly different across frontal intracortical depths was significant ($F = 14.69$; $p < 0.001$). In a complementary set of analyses, we calculated within-individual change in average frontal lobe R1 between longitudinal imaging timepoints, thereby deriving person-specific developmental estimates. Within-person increases in frontal cortex R1 were present in > 75% of individuals at all cortical depths, increased in magnitude with greater distance into the cortex, and decelerated in late adolescence (**Supplementary Fig. 2.2**). These analyses reveal robust longitudinal increases in R1 at the individual level and confirm convergence between group-level GAMM findings and within-person developmental effects.

Given evidence for heterochronous myelin maturation within the cortical ribbon of the entire frontal lobe, we sought to extend our investigation to individual frontal regions. To do so, we fit depth-specific GAMMs within each frontal region and studied differences in developmental timing across intracortical depths. The majority of frontal lobe regions showed significant increases in R1 ($p_{FDR} < 0.05$) at all cortical depths; the percent of significant regional effects increased with distance into cortex from 86% at superficial depth 1 to 99% at depth 7. In examining regional rates of R1 increase (**Fig. 2B**) and ages of R1 maturation (**Fig. 2C**) across depths, we discovered a consistent developmental pattern: when moving from superficial to deep cortex, the average rate of R1 developmental change increased, yet the age of R1 maturation decreased. Hence, with increasing cortical depth, age-related increases in R1 were larger in magnitude and were instantiated at a faster rate, yet R1 stabilized at younger ages. Although this depth-dependent pattern was present across the entire frontal lobe, there was variability across frontal regions in maturational rate and timing within a given depth (see depth-specific brain maps in **Fig. 2B-C**). Collectively, these analyses establish that myelin matures along a deep-to-superficial axis within the developing frontal cortex.

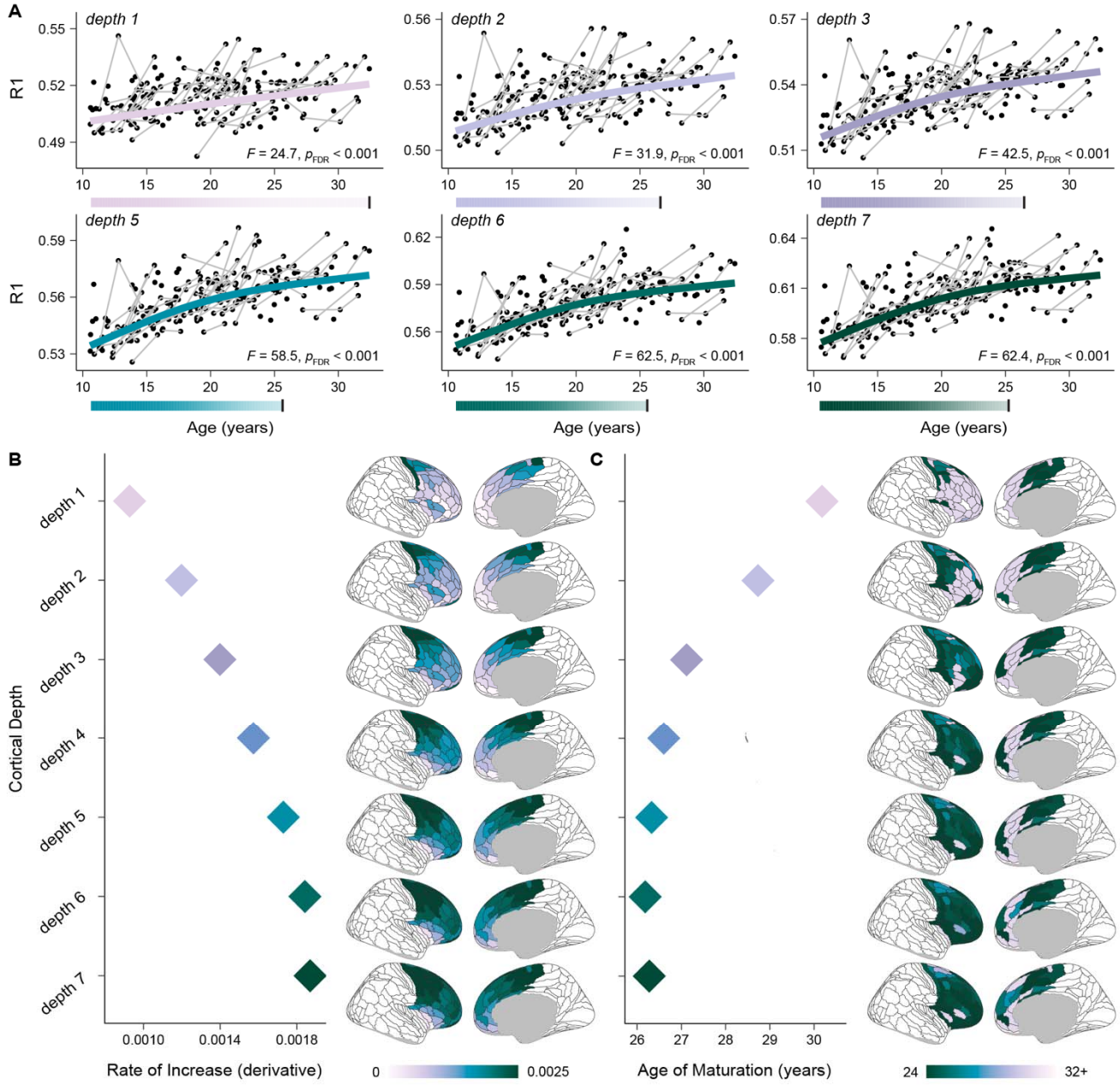

Figure 2. A deep-to-superficial axis of frontal cortex R1 maturation. A) Developmental trajectories of frontal lobe R1, modeled using GAMM smooth functions, are shown for 6 intracortical depths. Developmental trajectories are overlaid on participant-level data; longitudinal imaging sessions are connected. Growth bars demarcating age windows of significant R1 increase are also shown, shaded by the first derivative (Δ R1/Δ age) of the age spline. The *F*-statistic and the *p*-value of the age smooth term from each GAMM are indicated; *F*-statistics progressively increase in magnitude from superficial cortex (depth 1) to deep cortex (depth 7). B) The average rate at which R1 increased with age gets faster when moving from superficial to deep depths, indicative of larger magnitude developmental change in deeper cortex. Cortical plots (right) display the average rate of R1 increase in each frontal region at each depth. The corresponding depth plot (left) quantifies the average rate of R1 increase across all frontal regions at each cortical depth. The rate of increase was calculated as the average first derivative of the age spline across the age range studied. C) The age at which R1 matured in each region gets younger when moving from superficial to deep depths, suggestive of earlier maturational timing in deeper portions of cortex. Cortical plots (right) show the age of R1 maturation in each region at each depth. The depth

plot (left) quantifies the average age of maturation across frontal regions at each depth. The age of R1 maturation was operationalized as the youngest age at which the first derivative of the age spline was no longer significantly different from zero, based on a 95% simultaneous interval.

Frontal myelin matures hierarchically within cortical depths

Prior studies have demonstrated that reductions in developmental plasticity progress across cortical regions along a sensorimotor-association axis[3,5,8,9,12], facilitated, in part, by hierarchical increases in cortical myelin content[5,12–14,57]. We now aimed to assess the degree to which hierarchical myelination was characteristic of different intracortical depths, in order to characterize the patterning of plasticity in different portions of the cortical ribbon. We first assessed the extent to which myelin developed asynchronously across frontal regions within each intracortical depth by calculating the coefficient of variation for the rate of R1 increase across cortical regions. The coefficient of variation measures dispersion around the mean, with higher values indicative of higher variability. The coefficient of variation increased in a step-wise manner from the deepest depth to the most superficial depth (0.28, 0.31, 0.32, 0.38, 0.42, 0.45, 0.51 from depths 7 to 1). This ordered change denotes that deeper cortical layers show more uniform increases in R1 during youth, whereas superficial layers exhibit enhanced variability in R1 developmental change across regions. We next examined the extent to which this regional variability was explained by a cortical region's rank in the hierarchical S-A axis of cortical organization[3] (**Fig. 3A**). We observed negative correlations between rates of R1 increase and S-A axis ranks at all depths, signifying that the rate of myelination was always largest in primary and early motor cortices and progressively decreased across heteromodal and paralimbic prefrontal cortices. However, the strength of developmental alignment to the S-A axis steadily increased when transitioning from deep to superficial cortex (**Fig. 3B**) and thus was strongest in depth 1 (r = -0.51, $p_{SA\text{-}null}$ = 0.046; **Fig. 3C**)**.**

We theorized that hierarchically-organized heterogeneity in developmental myelination may reflect differences in regional cytoarchitecture across the frontal lobe. We therefore investigated whether variability in the rate of R1 increase at each intracortical depth was expressed along a main axis of cytoarchitectural variation that captures regional differences in depth-dependent histological staining profiles (**Fig. 3D**)[58]. Rates of R1 increase showed evidence of systematic coupling to cytoarchitectural variation, unveiling that differences in myelin growth patterns reflect differences in the size, packing density, and laminar distribution of neurons. Correlations between the rate of R1 increase and the axis of cytoarchitectural variation were strong across all depths (r > 0.54; **Fig. 3E**) and slightly stronger in superficial than in deep cortex (e.g. r = 0.64, $p_{SA\text{-}null}$ = 0.013 in depth 1; **Fig. 3F**). Altogether, these findings suggest that hierarchical maturation across cytoarchitecturally distinct cortical regions is present throughout the cortical ribbon and enhanced in superficial cortex.

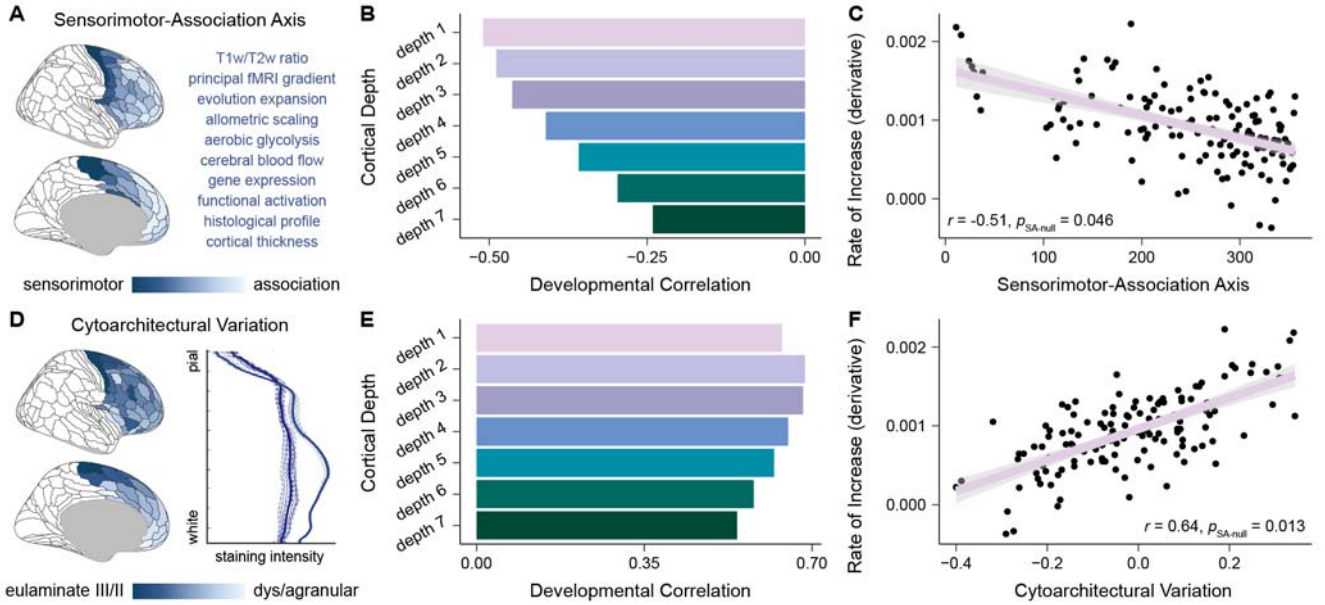

Figure 3. Hierarchical development of frontal R1 throughout the cortical ribbon. A) Each frontal lobe region is ranked along the sensorimotor-association (S-A) axis. The S-A axis is a hierarchical axis of cortical organization that captures the stereotyped patterning of feature heterogeneity from primary and unimodal cortices involved in perception and action (sensorimotor pole) to heteromodal and paralimbic cortices involved in executive and socioemotional processing (association pole). The S-A axis was derived in Sydnor et al.[3] by averaging rank orderings of the 10 listed cortical feature maps. B) Developmental correlations quantifying the association between regional rates of R1 increase (average first derivative) and regional S-A axis ranks within the frontal lobe are presented for each cortical depth. Correlations were negative, indicating that the average rate of R1 increase was largest at the motor pole of the frontal S-A axis and progressively declined towards its association pole. The strength of the negative correlation increased from deeper cortex (depth 7) to superficial cortex (depth 1). C) A scatterplot of the developmental correlation with the S-A axis for intracortical depth 1 illustrates hierarchical myelination of superficial cortices during youth. D) Each frontal lobe region is ranked along an axis of cytoarchitectural variation obtained by Paquola et al. [58] using the BigBrain 3D histological atlas, a post-mortem atlas of cell body staining. Cytoarchitectural variation was characterized by cross correlating depth-wise straining intensity profiles between different cortical locations, thereby indexing regional differences in neuron density and soma size throughout the cortical ribbon. Cytoarchitectural variation captures a continuum of cortical types along a eulaminate to dys/agranular axis characterized by decreasing laminar differentiation[15]. E) Developmental correlations quantifying the association between regional rates of R1 increase and position on the frontal axis of cytoarchitecture variation are shown for all depths. Correlations were positive, linking accelerated myelination to eulaminate cortices and slower myelination to dys/agranular cortices. F) A scatterplot of the developmental correlation with the cytoarchitectural axis is displayed for intracortical depth 1, highlighting differences in R1 development depending on a region's cytoarchitectural profile.

Depth-wise maturational profiles reflect functional diversity

Thus far, we have provided evidence for deep-to-superficial and hierarchical axes of cortical myelin development, which evolve simultaneously in the developing frontal cortex. We next endeavored to understand how these axes interact to govern depth-wise trajectories of myelin maturation within individual cortical regions. Visualizing R1 developmental profiles across all 7 depths in individual regions revealed a spectrum of depth-wise maturational patterns across regions of the frontal lobe (**Supplementary Fig. 4.1**). This spectrum ranged from regions with R1 age splines that plateaued simultaneously across intracortical depths, to those with heightened variability in the shape of depth-wise splines, to regions with relatively linear age splines in all intracortical depths. To provide further insight into the topography of these regional differences in maturational patterns, we identified zones of frontal cortex that exhibited similarly shaped trajectories of age-related change in

R1 across intracortical depths. To accomplish this, we first quantified the average curvature of each depth-specific developmental spline in all regions. We then determined how frontal regions naturally clustered based on their depth-wise curvature profiles and functionally decoded clusters using Neurosynth. We extracted three clusters from the curvature data with k-means, which differentiated three overarching modes of depth-wise R1 maturation (**Fig. 4A**).

The first cluster (light blue in **Fig. 4**) was comprised of a small number of regions necessary for motor control and coordination (**Fig. 4B**). Within this motor cluster, all intracortical depths exhibited an R1 developmental spline with high curvature that matured in the early to mid 20s (**Fig. 4D-E**), as exemplified by primary motor cortex (**Fig. 4C**, left). The second cluster (dark blue in **Fig. 4**) occupied the majority of the lateral prefrontal cortex and was composed of regions that support cognitive control and working memory (**Fig. 4B**). In this cognitive cluster, depth-wise maturational patterns mirrored those seen in the dorsolateral PFC (area 46 in **Fig. 4C**, middle). Mid-to-deep intracortical depths showed R1 splines with high curvatures that matured by the mid 20s, whereas superficial depths showed low curvature splines and protracted R1 increases until ages 28-30 years (**Fig. 4D-E**). Consequently, the second cluster included regions that displayed the greatest divergence in the shape of developmental curves between superficial and deep cortical depths (**Fig. 4F**)—localizing elevated laminar variability in R1 development to cognitive control regions. The third cluster (light purple in **Fig. 4**) included regions within the insula, medial prefrontal cortex, and anterior cingulate that were functionally linked to salience/arousal, decision making, and emotion regulation (**Fig. 4B**). Within this cluster, R1 splines were typified by low curvature and protracted R1 increases at all depths (**Fig. 4D-E**), as seen in the anterior cingulate (area a24 in **Fig. 4C,** right). These analyses highlight how the simultaneous temporal unfolding of deep-to-superficial and hierarchical developmental programs ultimately engender differences in the growth of a mechanistic regulator of plasticity across layers of functionally diverse cortical areas.

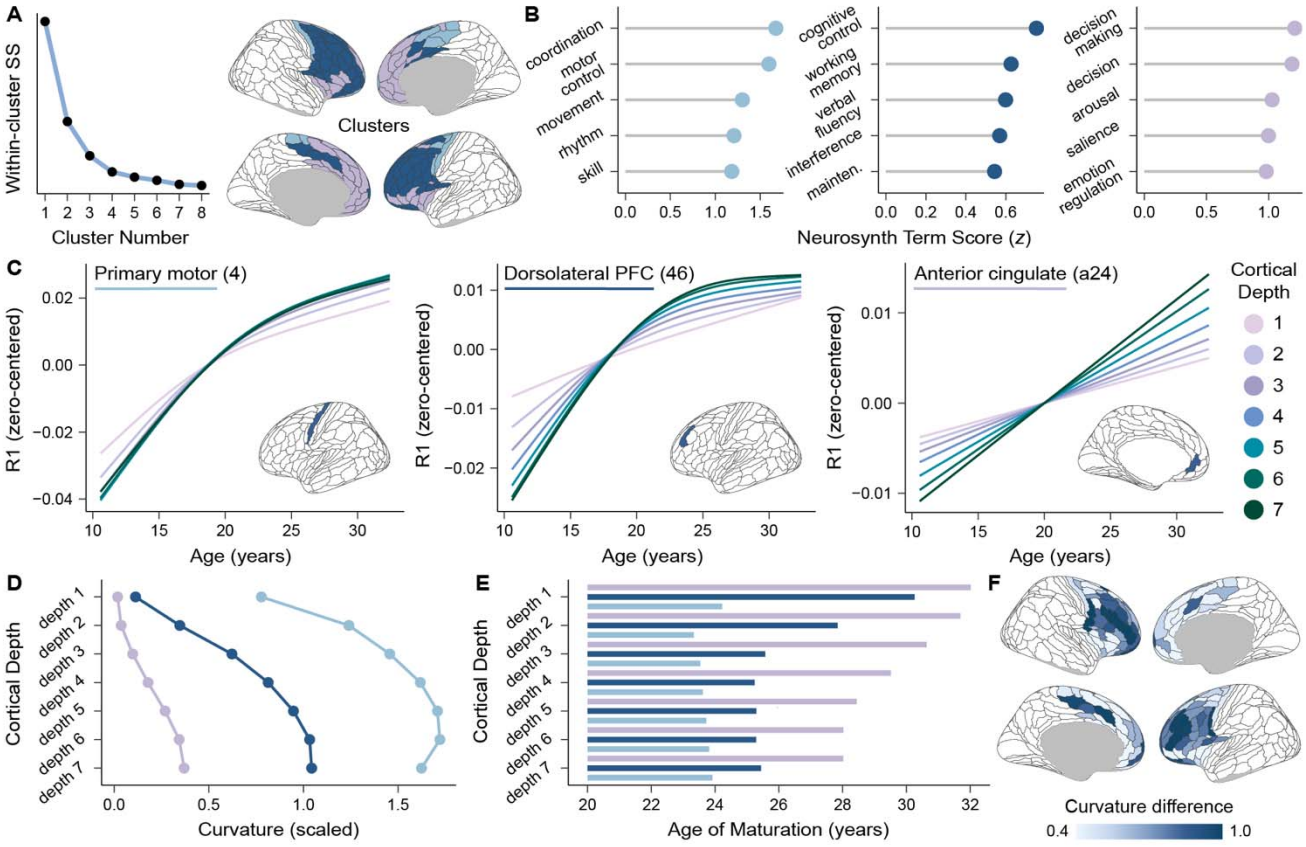

Figure 4. Depth-wise R1 maturational profiles diverge between functionally distinct cortical areas. A) A clustering analysis identified zones of the frontal lobe that exhibit similar R1 maturational profiles across all 7 intracortical depths. Clusters were identified by calculating the curvature of each region's 7 depth-dependent splines and applying k-means clustering to the curvature values. Three clusters were extracted based on the convergence of 30 indices for determining the optimal number of clusters; the suitability of a three-clustering solution was confirmed with a scree plot of the total within-cluster sum of squares (SS). B) Functional decoding of identified clusters classified motor, cognitive control, and salience/emotion clusters. The primary functions supported by cortical regions included in each of the clusters were identified using meta-analytic maps of over 100 psychological terms derived from Neurosynth. C) Developmental trajectories of R1 are shown for all 7 cortical depths in the primary motor cortex (area 4; left), the dorsolateral prefrontal cortex (area 46; middle) and the anterior cingulate cortex (area a24; right). Developmental trajectories are GAMM smooth estimates that are independently zero-centered along the y-axis. Regional plots illustrate three different modes of depth-dependent R1 change characteristic of motor, cognitive control, and salience/emotion clusters. D) Developmental spline curvature values are displayed for all 7 intracortical depths for each cluster. High curvature values, seen in all depths of the motor cluster and deep depths of the cognitive control cluster, reflect non-linear, curved splines that plateau. Low curvature values, characteristic of all depths in the salience/emotion cluster and superficial depths of the cognitive cluster, signify relatively more linear spline fits. E) The average age at which R1 matured is charted for all intracortical depths in each cluster. Ages of maturation got progressively older between motor, cognitive control, and salience/emotion clusters and showed the greatest depth-wise variability within the cognitive cluster. F) Cortical regions of the cognitive cluster generally exhibited the greatest difference in developmental spline curvature values between deep depths (4-7) and superficial depths (1-3), indicative of laminar variability in the shape of R1 trajectories. The difference in curvature values between deep and superficial depths is plotted on the cortex as the curvature difference.

Frontal myelination patterns are robust in sensitivity analyses

To ensure that the observed patterns of frontal cortex R1 development applied across sexes and were robust to potential biological or methodological confounds, we fit sex-stratified models and additionally performed a series of sensitivity analyses. R1 did not significantly differ between females and males in any region at any intracortical depth ($p_{FDR} > 0.05$ for the main effect of sex in all models), although there was a qualitative trend of females having higher R1 than males in superficial depths. R1 developmental splines also did not significantly differ by sex ($p_{FDR} > 0.05$ for all age-by-sex interactions), suggesting similar developmental trajectories in females and males. Moreover, when covarying developmental models for biological sex, depth-wise developmental patterns were unchanged (**Fig. 5i**).

We subsequently evaluated whether age-dependent changes in R1 within the frontal cortical ribbon replicated when covarying depth-specific GAMMs in each region for cortical thickness, cortical gyrification (indexed by mean curvature), structural data quality (indexed by the euler number), and cortical partial voluming (indexed by the cortex volume fraction). In all sensitivity analyses, R1 significantly increased in the vast majority of frontal regions (> 84%) at all intracortical depths. Moreover, in all of the sensitivity analyses performed, both depth-wise and regional patterns of the rate of R1 increase and the age of R1 maturation very closely mirrored results from the main analysis (**Fig. 5A-B**). Finally, regardless of the biological or methodological covariate included in sensitivity analyses, different modes of depth-wise R1 maturation could be seen within functionally diverse cortical regions (**Fig. 5C**) and clustering of cortical regions based on their depth-wise maturational profiles was highly stable (**Supplementary Fig. 5.1**). These analyses affirm that findings concerning regional and depth-wise R1 growth within the frontal cortex are consistent across sexes and are not driven by individual differences in cortical architecture or structural data quality.

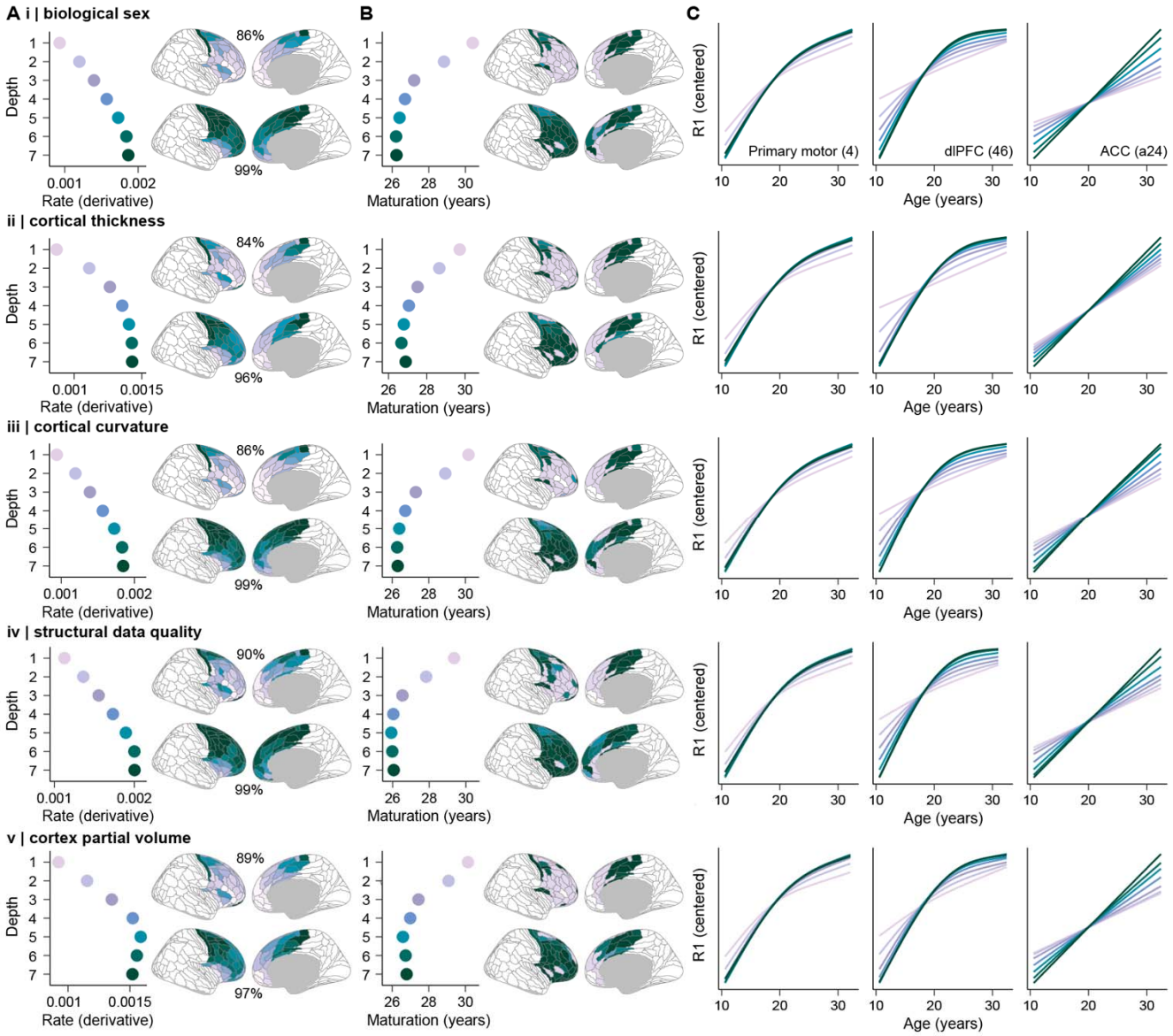

Figure 5. Developmental findings are robust in sensitivity analyses. Regional and depth-wise patterns of frontal cortex R1 development are robust to controls for individual differences in i) biological sex, ii) cortical thickness, iii) cortical curvature, iv) structural data quality, and v) cortex partial volume effects. Key results are shown for each of these five sensitivity analyses; all results strongly converge with findings from the main analysis. A) Depth plots display the average rate of R1 increase in the frontal lobe at each of the 7 intracortical depths (colored circles; average first derivative). The corresponding cortical maps present the average rate of R1 increase in each frontal region in the most superficial depth (1) and deepest depth (7). Percentages indicate the percent of frontal lobe regions that exhibited a significant increase in R1 at the corresponding depth. B) Depth plots chart the average age at which R1 matured in the frontal lobe at each of the 7 intracortical depths (colored circles; first age at which the derivative was no longer significant). The corresponding cortical maps show the age of R1 maturation in each frontal region in depths 1 and 7. C) Developmental trajectories of R1 at all 7 intracortical depths are shown for the primary motor cortex (area 4), the dorsolateral prefrontal cortex (dlPFC; area 46) and the anterior cingulate cortex (ACC; area a24).

Frontal cortex myelin supports E/I-linked neural dynamics

Continued myelination of the developing frontal cortex over the span of decades should have a profound, yet under-characterized, effect on cortical circuit physiology. Given that the majority of cortical myelin forms around afferent and efferent excitatory connections and inhibitory PV interneurons[24–26,59], we theorized that intracortical myelin would alter the local E/I ratio and E/I-linked neural dynamics. To test this theory, we related intracortical R1 to aperiodic EEG activity, which provides a readout of non-oscillatory, population-level neural activity. Computational, pharmacological, and neurochemical data have shown that decreases in the aperiodic exponent—a measure of how power decays with increasing frequency—reflect increases in E/I balance[60,61] and a faster timescale of neural activity[62,63]. We therefore specifically predicted that greater R1 in the cortex would be linked to a lower aperiodic exponent, providing evidence that myelin balances fast pyramidal[36] and PV neuron firing[36,49] to facilitate efficient, dynamical changes in population activity.

To map aperiodic activity derived from scalp EEG to specific areas of the frontal cortex, we created a surface-based atlas of EEG electrode positions (see Methods) and grouped electrodes that localized within four different cortical territories: the ventrolateral PFC, the dorsolateral PFC, the superior PFC, and the primary motor cortex (**Fig. 6A**). Replicating prior findings[61,64,65], the aperiodic exponent significantly declined with age (indicative of a flattening of the aperiodic slope; **Fig. 6B**) in all four cortical territories ($p < 0.001$ for all four age splines; **Fig. 6C**). To empirically study relationships between R1 and the aperiodic exponent, we quantified R1 in the surface-based EEG electrode atlas, thereby isolating R1 from cortical locations proximal to EEG electrodes. Given that pyramidal neurons in both superficial and deep cortical layers make major contributions to scalp-based EEG activity[66,67], we fit GAMMs to study relationships between the exponent and both superficial R1 (averaged in depths 1-3) and deep R1 (averaged in depths 4-7) while controlling for developmental effects. As predicted, higher R1 in deep cortex was significantly associated with a lower aperiodic exponent (flatter slope) in the ventrolateral PFC ($F = 5.50$, $p = 0.017$), dorsolateral PFC ($F = 4.26$, $p = 0.041$), superior PFC ($F = 4.52$, $p = 0.035$), and primary motor cortex ($F = 4.68$, $p = 0.032$). In contrast, higher R1 in superficial cortex was only significantly associated with a lower exponent in motor cortex ($F = 5.84$, $p = 0.017$). Superficial and deep cortex R1 were not significantly associated with the aperiodic offset, which is influenced by total neuronal spiking[68], suggesting that associations were specific to the temporal dynamics (rather than the level) of neuronal activity.

The above results intimated that associations between R1 and the exponent were stronger in deep than in superficial portions of the cortical ribbon for lateral prefrontal regions that exhibit divergent R1 trajectories across depths (**Fig. 6D**), yet similar in the primary motor cortex, which exhibits large R1 increases at all depths. We therefore fit GAMMs with a depth interaction term to formally test whether the R1-exponent relationship was stronger for R1 in deep than in superficial cortex. The depth interaction term was significant for the ventrolateral PFC ($F = 15.04$; $p < 0.001$; **Fig. 6E,** left), dorsolateral PFC ($F = 9.97$; $p = 0.002$), and superior PFC ($F = 6.97$; $p = 0.009$; **Fig. 6E,** right), but not the primary motor cortex ($F = 3.55$; $p = 0.061$). These findings replicated in a sensitivity analysis that used Brodmann areas to spatially relate cortical R1 to EEG activity (**Supplementary Fig. 6.1)**. Altogether, the present analyses indicate that greater R1, particularly within heavily myelinated and earlier maturing cortical locations, corresponds to the expression of an E/I-linked signature of fast cortical dynamics.

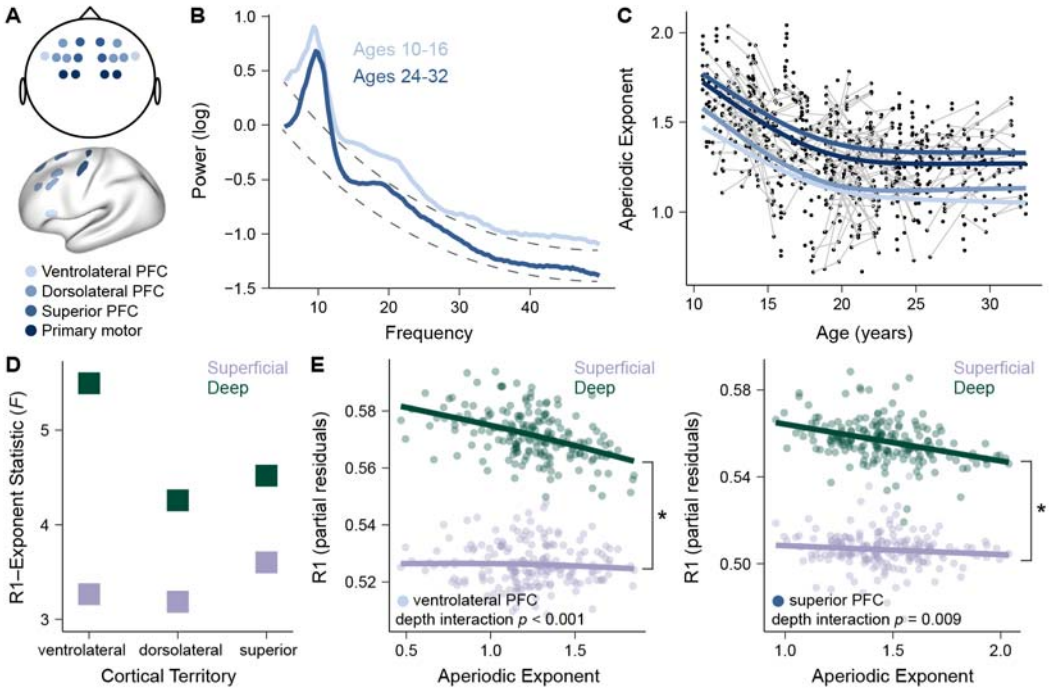

Figure 6. Frontal cortex R1 is associated with EEG-derived neural dynamics. A) Frontal EEG electrodes were mapped from the scalp to the cortex to derive a surface-based atlas of EEG electrode positions. Depth-dependent R1 and the aperiodic exponent were averaged across spatially proximal electrodes within the ventrolateral prefrontal cortex (PFC), dorsolateral PFC, superior PFC, and primary motor cortex. B) The aperiodic exponent was calculated from the slope of the 1/f power spectral density (approximated by the dotted line for illustration). The exponent quantifies how quickly power decays with increasing frequency. The average power spectrum across frontal electrodes is shown for individuals 10-16 and 24-32 years old. C) The aperiodic exponent decreased from age 10 to the early 20s in the ventrolateral PFC, dorsolateral PFC, superior PFC, and primary motor cortex. Developmental trajectories (GAMM-predicted exponent values) for all four territories are shown overlaid on participant-level data. Trajectories are colored according to the EEG electrode atlas in panel A. Trajectories were derived from GAMMs fit independently for each cortical territory prior to visualization in the same graph. D) Depth-specific GAMMs provide evidence for stronger associations of the aperiodic exponent with deep than superficial R1 across the lateral PFC. Independent GAMMs were fit to model relationships between the exponent and deep R1 or superficial R1 in each frontal territory, controlling for age. The *F*-statistic derived from the GAMM term relating the exponent to R1 is plotted. *F*-statistics are larger in deep than in superficial cortex. E) GAMMs with a depth interaction term reveal a significantly stronger negative association between R1 and the aperiodic exponent in deep as compared to superficial cortex. R1-exponent associations are shown for deep and superficial cortex in the ventrolateral PFC (left) and the superior PFC (right); data points represent partial residuals from a depth interaction model that controlled for age.

Frontal cortex myelin relates to learning and processing speed

In a final set of analyses, we calculated task-based measures of learning rate and processing speed to probe whether myelin in superficial “computation” layers and deep “output” layers supports unique aspects of efficient cognitive processing. We used data from a youth-friendly sequential decision-making task[69,70] that involved learning stimulus-outcome relationships to earn rewards in two task stages. Stages were characterized by fixed (stage 1) and dynamically changing (stage 2) stimulus-outcome probabilities (**Fig. 7A**). To operationalize learning, we applied a Bayesian reinforcement learning model to trial-level data and calculated participant learning rates on each stage of the task. To index processing speed, we calculated the average response time on each stage of the task. Both learning rates (*paired t* = 2.4, $p = 0.016$) and response times (*paired t* = 14.8, $p < 0.001$) significantly increased within-person between stages 1 and 2 of the task (**Fig. 7B**), signifying that

stage 2 elicited a faster speed of updating and slower decision making due to its changing (as opposed to stable) reward contingencies. Learning rates slightly but significantly increased with age in a linear fashion (stage 1: $F = 5.51$, $p = 0.020$; stage 2: $F = 8.81$, $p = 0.004$; **Fig. 7C**) and response times significantly decreased with age during the adolescent period (stage 1: $F = 29.98$, $p < 0.001$; stage 2: $F = 7.85$, $p = 0.005$; **Fig. 7D**).

As in the analyses linking R1 to EEG activity, we first averaged R1 in superficial (1-3) and deep (4-7) cortical depths and used GAMMs to study depth-specific relationships between R1 and cognitive measures while controlling for age. These depth-specific analyses provided initial evidence for the presence of significant relationships between R1 and task measures that were relatively stronger in superficial cortices. However, in GAMMs that tested for R1-cognition interactions by cortical depth, depth interaction terms were not significant in any frontal region for any cognitive measure ($p_{FDR} > 0.05$ for all interactions tested). We therefore combined across superficial and deep cortex for further analysis. Examining combined-depth associations between R1 and learning rates revealed that no frontal region showed a significant relationship between R1 and learning rate during stage 1 of the task (**Fig. 7Ei**). In contrast, during stage 2 of the task, faster learning rates were significantly associated with higher R1 in 25 of 135 frontal regions ($p_{FDR} < 0.05$). Significant regions localized primarily to the dorsolateral PFC (**Fig. 7Eii**) and comprised cortices activated by tasks that involve cognitive control, response selection, and reinforcement learning (**Fig. 7F**, based on Neurosynth decoding). Greater R1 in higher-order cognitive regions was thus linked to more dynamic learning during task stages characterized by stochastic—but not stable—environmental contingencies.

Combined-depth analyses relating R1 to response times showed that greater R1 throughout much of the frontal cortex was significantly associated with faster responding during both stage 1 of the task (54 significant regions at $p_{FDR} < 0.05$; **Fig. 7Eiii**) and stage 2 of the task (77 significant regions at $p_{FDR} < 0.05$; **Fig. 7Eiv**). We theorized that these anatomically distributed relationships may reflect the capacity for prefrontal myelin to enhance overall cognitive processing speed, rather than just the speed of motor outputs. To test this theory, we used combined-depth GAMMs to relate R1 to response times on an anti-saccade task—a prefrontal-dependent task that taxes inhibitory control—and a visually-guided saccade task—a task that gauges sensorimotor processing speed. This allowed us to compare results from the decision-making task to independent tasks of cognitive control and reflexive visual-motor responding. Faster responding on correct trials of the anti-saccade task was associated with significantly higher R1 across much of the frontal lobe (83 significant regions at $p_{FDR} < 0.05$). On the other hand, faster responding on the visually-guided saccade task was only significantly associated with higher R1 in 2 regions, including in the primary motor cortex. These specificity analyses (**Fig. 7G**) demonstrate that greater myelination of the prefrontal cortex supports faster processing speed specifically when endogenously engaging higher-order cognitive processes.

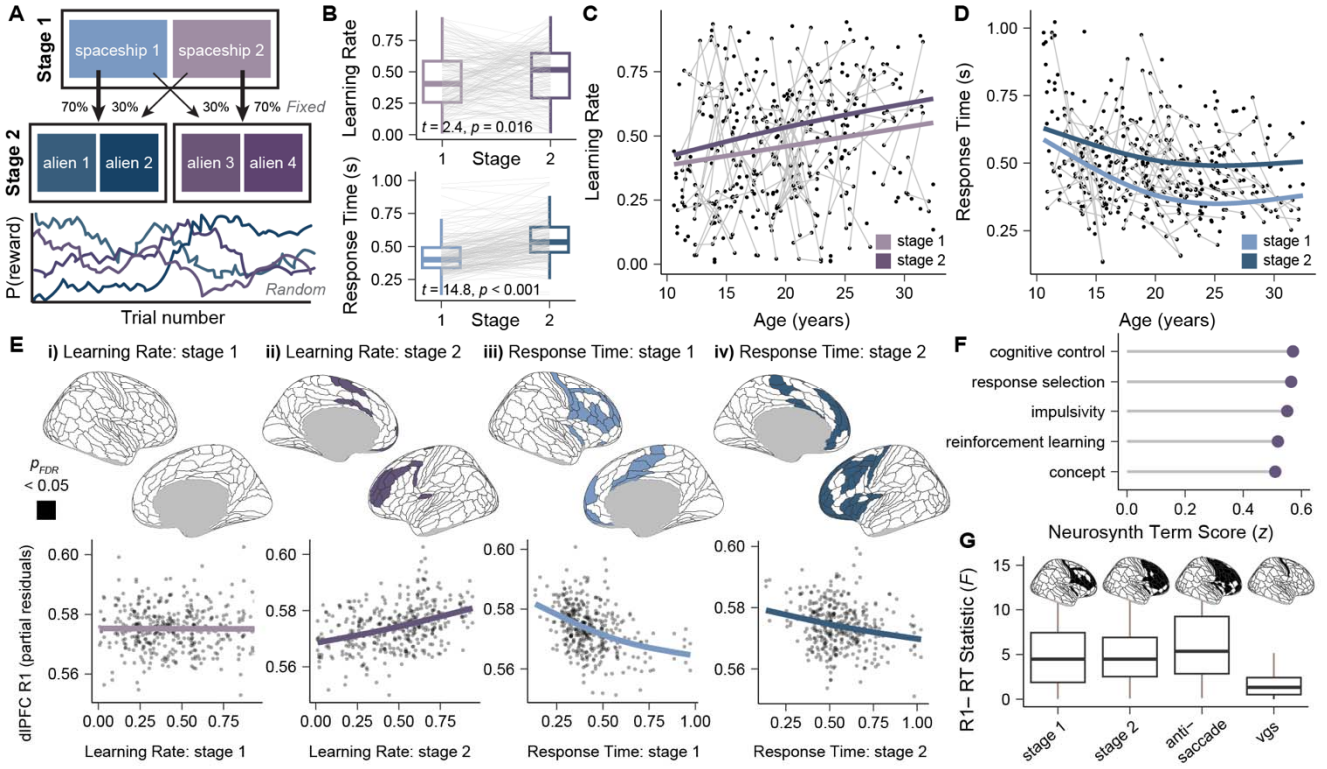

Figure 7. Prefrontal cortex R1 is linked to learning rate and processing speed. A) Participants completed a two-stage sequential decision-making task to earn rewards. During the first stage of each trial, participants selected one of two spaceships that transitioned with fixed probabilities to either a common planet (70% of transitions) or rare planet (30% of transitions). During the second stage of each trial, participants selected one of two aliens on the planet for the chance to receive a reward; the probability of receiving a reward (P(reward)) from each alien fluctuated randomly to incentivize continuous learning of changing contingencies. B) Learning rates and response times significantly increased within-person (grey lines) between stages 1 and 2 of the task, as assessed with paired-samples t-tests. C) Learning rates increased linearly with age on stage 1 and 2 of the task, although substantial inter-individual variability is present at all ages. D) Response times decreased non-linearly with age on stage 1 and 2 of the task. E) Cortical plots are shown that highlight frontal regions where across-depth R1 was significantly associated with i) stage 1 learning rates, ii) stage 2 learning rates, iii) stage 1 response times, and iv) stage 2 responses times. Significant regions are colored. Below each cortical plot, the relationship between each cognitive measure and R1 in the dorsolateral prefrontal cortex (dlPFC) is shown in a partial residual plot. F) Neurosynth-based functional decoding of brain regions that exhibited a significant association between R1 and stage 2 learning rates (purple regions in Eii) emphasizes their role in cognitive control, decision making, and reinforcement learning processes. G) Associations between frontal R1 and response times (RT) were larger when engaging higher-order cognitive control (stage 1, stage 2, anti-saccade) than when performing a simple visual-motor response (visually-guided saccade, vgs). The cortical brain plots highlight frontal regions with a significant relationship between R1 and task-specific response times; significant regions are in black. Boxplots summarize the distribution of regional *F*-statistics derived from GAMMs relating frontal R1 to RT on each task. Regional *F*-statistics are smaller for the vgs. Boxplot limits correspond to the first and third quantiles with whiskers extending up to 1.5x interquartile range.

Discussion

During the process of embryonic corticogenesis, layers of the cerebral cortex form in an inside-out manner; ex vivo studies have shown that progressively more superficial layers (with the exception of layer 1) experience later windows of neurogenesis and laminar differentiation[71]. In the current study, we demonstrate *in vivo* that the maturation of myelin shows a similar temporal sequence during adolescence. In doing so, we extend a fundamental principle of prenatal cortical formation to postnatal cortical plasticity. Specifically, we found that myelin-sensitive R1 matures along a deep-to-superficial axis in the developing frontal lobe, with progressively more superficial depths exhibiting shallower and more protracted increases in R1 than deeper cortices. This axis unfolds simultaneously with a hierarchical axis of R1 development across frontal regions, leading to different profiles of depth-wise maturation between cytoarchitecturally and functionally distinct areas. By combining quantitative myelin imaging with measures of EEG aperiodic activity, we uncovered that higher R1 in predominantly deeper cortical depths was related to a functional index of higher E/I balance[60,61] and a faster timescale of activity[62,63]. Finally, using tasks of decision making, inhibitory control, and oculomotor saccades, we linked higher R1 in both deep and superficial depths of the lateral PFC to enhanced learning rates and faster cognitive—but not sensorimotor—processing speed. Together, these results provide evidence for asynchronous reductions in plasticity in deep "output" layers and superficial "computation" layers of the PFC. This asynchronous maturation likely allows higher-order association cortex to co-express stability and malleability at different stages of layer-stratified cognitive processing hierarchies.

The deep-to-superficial axis of prefrontal R1 maturation provides insight into laminar variation in intracortical myelination trajectories. In deeper cortical depths proximal to layers 5/6, increases in R1 were larger, plateaued earlier, and occurred relatively more synchronously across regions. In superficial depths that localize approximately to layers 2/3, increases in R1 were shallower, protracted, and expressed with heightened topographic variability. These data provide evidence for greater myelination and earlier maturation of layer 5/6 cortical-subcortical and feed-back cortical projections, coupled with temporally extended myelination of layer 2/3's highly integrative cortico-cortical circuitry[19,72]. Preferential myelination of deep cortex may function to consolidate top-down connectivity earlier during youth, ensuring that pyramidal cells that produce behavioral outputs propagate signals reliably and quickly. In contrast, shallow yet continued myelination of superficial cortex likely allows high-dimensional computational circuits to retain enhanced flexibility important for continued learning and memory[36,73]. Indeed, microscopy studies have shown that less densely myelinated axons have a greater number of afferent and efferent synapses[59] and myelin sheaths that remodel more extensively in adulthood[35], making these axons a locus for continued synaptic and myelin plasticity.

Heterochronous R1 maturation may reflect differences in the degree to which layer-specific myelination arises from innate versus experience-dependent processes[33,73,74]. Myelin formation is stimulated by both innate, activity-independent genetic programs and experience-dependent increases in neuronal activity[33,59,73,75,76]; these processes may be more prominent, respectively, in deep and superficial cortices. Although oligodendrocyte precursor cells are evenly dispersed throughout cortical layers, myelinating oligodendrocytes increase in density in layers 5/6[59,75]—even when the laminar position of these layers is manipulated genetically[59,77]. This cell type pattern is thought to emerge due to an intrinsic capacity for pyramidal neurons in deep layers to stimulate oligodendrocyte differentiation and myelination relatively independent of activity. In contrast, activity-dependent myelination may be more prominent in superficial layers. Layers 2/3 contain pyramidal cells that engage in highly recurrent excitatory activity[19,20]. Furthermore, these layers wrap a substantially greater proportion of total myelin around PV interneurons, which undergo activity-dependent myelination in response to environmental inputs[78,79]. Accordingly, the shift from earlier-maturing, synchronous R1 increases in deep cortex to prolonged, spatially variable R1 increases in

superficial PFC may reflect a transition from genetically-programmed to extrinsically-driven myelin formation.

In addition to uncovering laminar heterochronicity in R1 maturation, we identified regional variability in the nature of R1 development. R1 increased at a progressively slower rate along an anatomically-embedded frontal cortex hierarchy, indicative of greatest myelination in motor cortex and least myelination in paralimbic cortex. This pattern of developmental myelination, which was enhanced in superficial depths, coheres with ample evidence for a dominant, sensorimotor-association axis of experience-dependent developmental plasticity[4,5,8,9,12,80]. The stronger expression of this myelination pattern in superficial cortex furthermore indicates that a core feature of human neurodevelopment—the hierarchical cascading of plasticity—is enhanced in layers 2/3. The concurrent unfolding of laminar and hierarchical developmental axes ultimately resulted in motor, lateral prefrontal, and medial prefrontal/cingulate areas showing different depth-dependent growth of a regulator of plasticity. Notably, the lateral PFC exhibited the greatest across-depth variability in the shape of R1 developmental trajectories. The lateral PFC also underwent maximal evolutionarily expansion in humans[81,82], driven by the expansion of layers 2/3[17]. Speculatively, it is possible that laminar variation in maturational timing is more regionally widespread in the brain of humans as compared to other primates due to the evolutionary elaboration of superficial cortices.

Although prolonged myelination of the cortex is a hallmark of postnatal development, how it impacts the function of local cortical circuits remains an active area of exploration. We found that greater R1 in primarily deeper cortices was associated with a smaller exponent of the aperiodic component of EEG, linking higher myelin content, particularly in layers 5/6, to more mature patterns of activity[61,65]. The aperiodic exponent decreases with a desynchronization of population-level firing[83] that results in faster temporal fluctuations in (i.e., a faster timescale of) activity[62,63]. The aperiodic exponent is also modulated by local E/I interactions[60,61], together suggesting that myelination of pyramidal and PV cells may quicken activity dynamics[49] to allow mature circuits to signal with higher temporal efficiency. Rapid, dynamical changes in activity may be more relevant to deep layers that produce temporally precise outputs[20,84] than to superficial layers that leverage persistent and recurrent activity[19,20]. Indeed, laminar electrode recordings have found that the aperiodic exponent decreases from superficial to deep cortex, reflecting a faster timescale of activity in layers 5/6 than in 2/3[63]. In conjunction with the present findings, these data suggest that developmental and laminar shifts in activity patterns may be partly engendered by a gradient of myelin density.

Rodent studies have demonstrated that activity-dependent myelin sheath formation occurs in the cortex on learning-activated axons[37,38]. Myelination may help to facilitate learning by fine-tuning population dynamics in a manner that allows circuits to adjust to new information more quickly, facilitating adaptability. In support of this theory, we found that higher R1 within the dorsolateral PFC was associated with a higher learning rate, a behavioral measure of cognitive updating speed. Strikingly, R1 was associated with learning rate in the context of stochastically changing, but not deterministic, environmental contingencies, suggestive of a role for dorsolateral PFC myelin in updating specifically when task performance demands a higher level of flexibility. In a complementary set of analyses, we observed that R1 throughout the PFC was associated with faster responding when engaging higher-order cognitive control—but not lower-order visuomotor processes—relating prefrontal myelin to processing speed with domain specificity. Contrary to our hypotheses, we did not identify statistically differentiable relationships between behavioral measures and R1 in superficial versus deep PFC. This lack of depth-dependent variation may reflect the fact that ultimately, behavior on cognitive tasks requires the integration of, and communication between, layer 2/3 and 5/6 circuitry. Accurate performance on working memory tasks, for example, requires activity in superficial layers for the manipulation and retrieval of information followed by activity in deep layers for the production of a behavioral output[84,85]. Myelin in superficial and deep layers could thus make differential contributions to distinct cognitive operations while jointly supporting overall task performance.

This study incorporates methodological innovation through the use of 7T MRI, quantitative myelin-sensitive imaging, and intracortical depth profiling; however, there are several methodological

limitations. First, equidistant depth sampling can be used to differentiate between deep and superficial depths that approximate layers 5/6 and 2/3, but it does not identify individual cortical layers. Second, the spatial resolution of the R1 data used here is not sub-millimeter, although it is equivalent to the resolution used in prior studies that sampled myelin-sensitive imaging measures at 10 or more cortical depths[11,41]. Given that sharp changes in laminar myelin profiles (e.g. turning points at layer boundaries) are smoothed at resolutions above 0.5 mm[86], smoothing or blurring of the R1 signal across spatially proximal depths is expected. Third, the spatial resolution of scalp EEG is inherently limited and EEG cap placement varies based on head shape. We aimed to co-localize EEG activity and R1 using a surface-based electrode atlas, but better source localization with EEG requires higher density electrode arrays and is still limited by signal spread across the scalp. Fourth, due to the instrumental use of ultra-high field and quantitative MRI, the size of the study sample is considerably smaller than many publicly available imaging samples collected at 3T, although the sample is one of the largest pediatric 7T samples collected to date.

During childhood and adolescence, the maturation of the human cortex is governed by large-scale spatial axes that organize the temporal unfolding of plasticity across cortical regions[3,8,9,12,23,28,80]. The current study demonstrates that a laminar axis of maturation additionally evolves throughout youth within the prefrontal cortical ribbon, revealing a unique aspect of human developmental chronology. Divergent maturational timing across deep and superficial layers is an underrecognized mechanism through which late-developing association cortices balance increases in circuit robustness with protracted adaptability. Critically, extended malleability in superficial layers may increase their susceptibility to developmental and environmental insults—contributing to an outsize role of layer 2/3 circuits in transdiagnostic psychopathology[52,87,88]. Moving forward, continued elucidation of the regional and laminar progression of plasticity will increase our understanding as to when specific cortical circuits experience demarcated windows of vulnerability and opportunity.

Methods

Developmental dataset

This study analyzes data from a healthy, accelerated longitudinal youth sample recruited from the greater Pittsburgh area by the Laboratory of Neurocognitive Development at the University of Pittsburgh. Individuals in this sample participated in one to three longitudinal sessions scheduled approximately 18 months apart. Each session consisted of three visits, including a cognitive testing visit, a 7T MRI visit, and an EEG visit, which typically occurred on different days over the course of a few weeks. Study exclusion criterion included contraindications to receiving an MRI, an IQ below 80, a history of loss of consciousness due to head injury, a history of substance abuse, and a history of major psychiatric or neurological conditions for the participant or a first-degree relative. All individuals over the age of 18 years gave written informed consent before study participation. Individuals under the age of 18 gave informed assent along with written parental consent. Participants received monetary compensation for participation in the study. All study procedures were approved by the Institutional Review Board at the University of Pittsburgh.

Following data quality exclusions (see Sample construction below), data from 140 individuals and 215 longitudinal imaging sessions were included in this study (85 individuals with 1 session, 35 individuals with 2 sessions, 20 individuals with 3 sessions). Participant demographics included an age range of 10 to 32 years (mean age = 20.0 years ± a standard deviation of 5.4 years) and a self-reported sex assigned at birth breakdown of 70 females and 70 males. Participants (18 years and older) or their parents identified the study participant's race/ethnicity: 8.6% of participants identified as Asian, 15% as Black, 2.9% as Hispanic, 67.1% as White, and 5.7% as multiracial; data were missing for 1 participant (remaining 0.7%). National percentile rankings of the area deprivation index for this study sample ranged from 3rd percentile to 99th percentile with a mean of 50.0 (± 25.6).

MP2RAGE acquisition

All MRI data were acquired on a single 7 Tesla Siemens Magnetom (MR B17) with parallel transmission (pTx). A Magnetization Prepared 2 Rapid Acquisition Gradient Echoes (MP2RAGE) sequence was collected and used to generate both a T1-weighted uniform (UNI) image and a quantitative T1 map, which were collectively used for intracortical myelin mapping. MP2RAGE sequences combine two gradient-recalled echo (GRE) images acquired with short (INV1; a predominantly T1w image) and long (INV2; a predominantly PDw image) inversion times. The combination of these images results in UNI and quantitative T1 images that are virtually free of B_1^-, proton density, and T2* effects and that have minimal B_1^+ transmit field inhomogeneity[89]. MP2RAGE data were acquired with an in-plane GRAPPA acceleration factor of 4 and the following parameters: inversion times of 800 ms (INV1) and 2700 ms (INV2), repetition time of 6000 ms, echo time of 2.87 ms, flip angles of 4 degrees (INV1) and 5 degrees (INV2), and a voxel resolution of 1 mm isotropic. Denoised UNI images with suppressed background noise were generated from this protocol using a robust (i.e., regularized; lambda = 10) combination of the two inversion time images[90]. Given the presence of enhanced B_1^+ field inhomogeneity present at ultra-high field strengths, MP2RAGE data were collected with a parallel transmit system to increase B_1^+ homogeneity and with an optimized protocol previously shown to minimize the sequence's B_1^+ sensitivity[91].

MP2RAGE-based cortical myelin imaging

MP2RAGE sequences generate inherently co-registered UNI and quantitative T1 images. The UNI image can be used as a T1w image for segmentation and cortical surface reconstruction given its high gray-white contrast and contrast-to-noise ratio (CNR)[92]. The T1 map provides a direct quantitative readout of the longitudinal relaxation time in seconds. The longitudinal relaxation time represents the time it takes for the longitudinal magnetization to return to equilibrium along the direction of the main magnetic field, typically ranging from approximately 1.4 to 2.2 seconds in gray matter[91]. Due to the fact that the largest influence on T1 relaxation is the presence of lipids, which are

both greatly enriched in and primarily accounted for by myelin[93], the T1 map can be used for R1 (1/T1; longitudinal relaxation rate) myelin imaging. The presence of myelin reliably shortens the T1 relaxation time and correspondingly increases the longitudinal relaxation rate; as a result, R1 is higher in areas with greater myelin content[53,94,95]. R1's sensitivity to cortical myelin concentration has been validated in multiple studies using anatomical mapping and post-mortem histology[44–47,95,96]. Furthermore, cortical R1 has been shown to have high CNR and excellent within-individual scan-rescan reliability at 7T, making it a valuable measure for use in longitudinal studies[48].

UNI images and quantitative T1 maps were processed with the goal of mapping R1 values to different locations in the cortical surface. First, to mitigate the potential effects of residual B_1^+ transmit field inhomogeneity on the acquired structural data, the UNICORT (unified segmentation based correction of R1 brain maps for transmit field inhomogeneities) algorithm[97] was applied to both denoised UNI images and raw quantitative T1 maps. UNICORT uses a probabilistic framework for simultaneous image segmentation, registration, and bias correction and was applied to UNI and T1 data using a containerized version of a statistical parametric mapping (SPM12) BIDS app. After UNICORT correction, UNI images were processed with FreeSurfer's longitudinal processing stream to generate individual-specific cortical surfaces. FreeSurfer with run using a containerized FreeSurfer BIDS app (FreeSurfer version 7.4.1). Longitudinal FreeSurfer creates a within-participant template using robust, inverse consistent registration and initializes final structural processing using common information from the template[98]. This ensures that segmentation and surface reconstruction are performed consistently across, and unbiased to, individual timepoints, thereby enhancing longitudinal reliability[98].

To enable cortical R1 mapping, volumetric R1 maps were computed from quantitative T1 images (R1 = 1/T1 in sec^{-1}) using 3dcalc from AFNI (version 23.1.10). R1 was then sampled to each participant's timepoint-specific cortical surface using FreeSurfer's volume-to-surface projection. R1 was sampled to surface vertices at 11 intracortical depths between the pial boundary and the gray-white boundary based on the relative fraction of cortical thickness. This allowed for the quantification of R1 at depths between 0% of cortical thickness (pial boundary) and 100% of cortical thickness (gray-white boundary) in 10% increments. Calculating depths based on percent of thickness ensures that R1 is sampled the same fraction into the cortex in all cortical regions, regardless of the region's total cortical thickness. While a direct mapping between each cortical depth and specific cortical layers cannot be made, a general distinction between more superficial cortex (depths closer to the pial boundary) and deep cortex (depths closer to the white matter boundary) can be drawn. Furthermore, given that the relative proportion of the cortical ribbon occupied by different layers has been described, approximate links can be drawn between depths <10% into cortex and layer 1, depths 10-45% into cortex and layers 2/3, and depths 65-100% into cortex and layers 5/6[19,43], with the percent depth of layer 4 being notably variable across regions[99].

After projecting R1 to different depths of cortex at the vertex-level, we quantified average R1 at each depth in individual cortical regions defined by the Human Connectome Project multi-modal parcellation (HCP-MMP)[100]. The HCP-MMP atlas was transformed from the fsaverage template to participants' timepoint-specific cortical surfaces using FreeSurfer's surface resampling algorithm, which employs spherical registration. Finally, we took analytic steps to ensure that we only analyzed R1 from cortical locations with 1) minimal to no partial voluming and 2) high quality R1 signal. To index partial voluming, we used participants' FreeSurfer-processed UNI images and tissue class segmentations to calculate the cortex volume fraction for every vertex at all 11 intracortical depths. The cortex volume fraction quantifies the fraction of the signal estimated to come from cortical gray matter (as opposed to white matter, subcortical gray matter, or CSF). We only analyzed 7 cortical depths where the average cortex volume fraction was > 90%; these 7 depths ranged from 20% of cortical thickness (depth 1) to 80% of cortical thickness (depth 7). To index signal quality, we computed the signal-to-noise ratio (SNR) of R1 in every HCP-MMP region, averaged across the 7 analyzed depths. We excluded 24 cortical regions in the temporal pole and medial prefrontal cortex

with low (< 20) SNR from all analyses. SNR was calculated as the vertex-wise mean of R1 divided by the standard deviation of R1 across all vertices included in a region.

Sample construction

At the start of this study, identical parameter MP2RAGE scans (i.e., non-variant acquisitions as assessed with CuBIDS software[101]) were available for 264 imaging sessions collected from 159 participants. These data underwent additional curation to ensure that only highly quality neuroimaging data were analyzed. Data were excluded from this initially collected dataset for the following reasons: UNI images or R1 maps failed visual quality control for motion or scanner artifacts (44 scans excluded), imaging data were collected within 6 months of an included session (4 scans excluded), and the R1 map had a whole-cortex mean R1 > 4 standard deviations above the group-level mean of eligible scans (1 scan excluded). This sample construction procedure, which included both qualitative and quantitative quality assurance steps, led to a final dataset of 215 longitudinal sessions collected from 140 individuals.

Brain maps of cortical anatomy, gene expression, and function

This study integrated previously published brain maps of cortical anatomy, gene expression, and function in order to validate MP2RAGE-based myelin mapping, contextualize developmental patterns, and perform functional decoding. The following cortical maps were used; each cortical map was obtained at the vertex-level and parcellated with the HCP-MMP surface atlas using Connectome Workbench version 1.5.

The sensorimotor-association axis of cortical organization

The S-A axis is a dominant axis of cortical organization that summarizes the stereotyped patterning of feature variability across a macroscale cortical hierarchy. The S-A axis was derived by Sydnor et al.[3] by combining 10 multi-modal and multi-scale cortical feature maps that exhibit systematic spatial variation between primary sensorimotor cortices and transmodal association cortices.

Myelin basic protein gene expression

A cortical map of myelin basic protein gene expression was produced by Wagstyl et al.[55] by processing postmortem microarray data from the Allen Human Brain Atlas. Of note, Wagstyl et al. generated and validated dense, across-donor gene expression maps for the left cortical hemisphere only, thus right hemisphere data are not included.

Myelin water fraction map

The myelin water fraction is derived from a quantitative, multi-echo assessment of T2 relaxation and represents the fraction of total water signal that is trapped between myelin bilayers. The group-average myelin water fraction map used in this work was generated by Liu et al.[56] by applying myelin water imaging to a sample of 50 healthy individuals ages 17 to 42 years old. The map from Liu et al. was obtained in MNI space and projected to the fsaverage surface using neuromaps 0.0.4 prior to parcellation with the HCP-MMP atlas.

A histology-based axis of cytoarchitectural variation

The axis of cytoarchitectural variation captures regional differences in depth-wise cytoarchitectural properties and spans from eulaminate cortex to dysgranular and agranular cortex. The cytoarchitectural axis was derived by Paquola et al.[58] using depth-wise cell body (Merker) staining intensity profiles from the BigBrain 3D histological atlas. Diffusion map embedding was applied to a region-by-region correlation matrix of depth-wise staining intensity profiles (sampled at 50 intracortical depths) to identify eigenvectors of cytoarchitectural differentiation.

Neurosynth meta-analytic maps of functional diversity

Neurosynth[102] collates data from over 15,000 previously published task-based functional MRI studies to facilitate coordinate-based meta-analyses of specific psychological terms. Meta-analytic maps derived from Neurosynth can be used to functionally decode groups of brain regions in terms of the mental processes that they support. We used the Neuroimaging Meta-Analysis Research Environment (NiMARE)[103] to compute meta-analytic activation maps from version 0.7 of the Neurosynth database. In accordance with prior work on functional decoding[104,105], we created meta-analytic maps for 123 psychological terms that were both available in Neurosynth and included in the Cognitive Atlas[106], an ontology of cognitive neuroscience concepts. Term-specific meta-analytic activation maps were computed with NiMARE in volumetric space using the multilevel kernel density Chi-square analysis. Values in these meta-analytic maps are association test *z* values that quantify the degree to which activation in a given cortical location occurred more consistently in prior task-based functional MRI studies that mentioned a given term as compared to those that did not. Term-specific meta-analytic activation maps were mapped to the fslr 32k cortical surface, parcellated with the HCP-MMP atlas, and z-scored across cortical regions for analyses.

Anatomical characterization

To determine whether across-cortex regional variation in R1 was hierarchically organized and coupled to independent maps of cortical myeloarchitecture, we averaged R1 across depths within each HCP-MMP region and computed correlations between the resulting R1 map and 1) the S-A axis, 2) the myelin basic protein gene expression map (left hemisphere only), and 3) the myelin water fraction map. Non-parametric Spearman's rank-based correlations were used to assess monotonic relationships between these brain maps. The significance of each Spearman's correlation was assessed with a conservative spatial autocorrelation-preserving null ($p_{SA\text{-}null}$) using the BrainSMASH software version 0.11.0[107]. BrainSMASH facilitates generative null modeling by producing surrogate (synthetic) brain maps with spatial autocorrelation that matches the degree of autocorrelation present in an empirical brain map. We used BrainSMASH to generate 1,000 surrogate maps that matched the spatial autocorrelation of the empirical R1 map; the autocorrelation structure of the surrogate maps was validated by comparing surrogate and empirical variograms. Surrogate maps were then correlated with the S-A axis, the myelin basic protein gene expression map, and the myelin water fraction map to generate a null distribution of Spearman's correlation values that was compared to the empirical R1 correlation. The $p_{SA\text{-}null}$ value is computed as the number of times the correlation with a surrogate map is greater than (for positive empirical correlations) or less than (for negative empirical correlations) the empirical Spearman's correlation value, divided by 1,000.

Developmental analyses

Developmental modeling

We used GAMMs (semiparametric additive models) with penalized splines to characterize developmental change in R1 throughout different regions and depths of the cortical ribbon. All GAMMs were fit using the mgcv package in R[108]. For regional analyses, GAMMs were fit independently to data from each HCP-MMP region. GAMMs allow for the characterization of both linear and non-linear age-dependent relationships by modeling age fits as flexible smooth functions (i.e., age splines) derived from a linear combination of weighted basis functions. Developmental GAMMs were fit with depth-specific R1 as the dependent variable and age as a smooth term with a random intercept per participant. The smooth term models the group-level developmental trajectory of R1 at a specific intracortical depth. Thin plate regression splines were used as the smooth term basis set and the restricted maximal likelihood approach was used for selecting smoothing parameters. To prevent overfitting of the age smooth function, a maximum basis complexity (k) of 4 was used and spline wiggliness was penalized. The significance of the smooth term *F*-statistic represents the significance of the developmental effect. When examining the significance of developmental effects across multiple frontal lobe regions, the false discovery rate correction was used to correct *p*-values

for multiple comparisons (designated as p_{FDR}) across all regions within a depth. In addition to the main developmental models, a GAMM with an age-by-depth interaction term was additionally fit for R1 averaged across the frontal lobe to test whether frontal cortex age splines significantly differed across the 7 intracortical depths. This age-by-depth interaction GAMM was fit with depth-wise R1 as the dependent variable, smooth terms for age and depth, a tensor product (continuous-by-continuous) interaction between age and depth, and a random intercept per participant nested within depth. The significance of the tensor product interaction designates whether developmental fits significantly varied across depths of the cortical ribbon.

To parameterize differences in the magnitude and timing of development across frontal lobe regions and depths, we extracted quantitative information regarding R1 development from age splines. Specifically, we calculated the average rate of R1 increase and the age of R1 maturation from the first derivative of the fitted age spline. All derivative analyses were implemented using the gratia package in R[109]. The first derivative of the spline was calculated with finite differences at 200 equally spaced age intervals, providing age-specific rates of developmental change. The average first derivative was then computed to index the average rate of R1 change across the spline; a greater average derivate is indicative of greater overall developmental change in the age range studied. To determine the age of R1 maturation, we identified the youngest age at which the first derivative was no longer significantly different than 0 by obtaining a simultaneous 95% confidence interval for the first derivative. This represents the age at which the rate of developmental change in R1 can no longer be statistically differentiated from 0 (two-sided). Developmental spline fits, rates of R1 increase, and ages of R1 maturation were used to understand the temporal unfolding of cortical development within the cortical ribbon.

Alignment to hierarchical and histological axes

In addition to studying age-related change in R1 across frontal cortical depths, we sought to characterize variability in R1 development across frontal regions within each intracortical depth. This allowed us to simultaneously explore axes of development within and across cortical regions in a depth-sensitive manner. We hypothesized that regional variability in R1 development would align with the S-A axis and the histology-based axis of cytoarchitectural variation, given prior evidence that cortical plasticity is refined hierarchically in youth[3,5,9,12] and decreases with progressive laminar elaboration[52]. To assess these hypotheses, we used Spearman's correlations to relate both the S-A axis and the cytoarchitectural axis to regional rates of R1 increase within each of the 7 intracortical depths, producing depth-specific correlation values. BrainSMASH was used to calculate the significance ($p_{SA\text{-}null}$) of these correlations at individual depths.

Clustering of depth-wise developmental trajectories

To identify groups of frontal regions that exhibit similar trajectories of R1 development across intracortical depths, we grouped regions with k-means clustering based on their depth-wise developmental profiles. The goal of this data-driven clustering analysis was to reduce the dimensionality of the depth-wise developmental data and understand overarching modes of intracortical myelin maturation (rather than to delineate definitive cortical boundaries based on myelin development). We clustered regions based on the shape of their R1 developmental splines across all 7 cortical depths by calculating the average curvature of the spline at each depth. Curvature provides a measure of how fast a curve is changing direction at a given point, and thus how much it deviates from a straight line. In the present context, higher average curvature values designate quadratic-plateauing splines whereas low average curvature values indicate that splines are closer to linear. In order to determine the number of curvature-based clusters to identify with k-means, we used the NbClust package in R[110]. NbClust determines the optimal clustering scheme across 30 different indices for determining the number of clusters present in a dataset. We considered clustering schemes comprised of 2 to 8 clusters. Based on majority rule across all 30 indices, 3 was identified as

the most apposite cluster number. The appropriateness of 3 clusters was confirmed with a scree plot of the total within-cluster sum of squares.

After identifying cortical clusters with shared developmental features, we summarized these features by calculating 1) the average curvature of the age spline at each depth across all regions in a cluster and 2) the average age of R1 maturation at each depth across all regions in a cluster. We additionally performed functional decoding with Neurosynth to identify the primary behavioral functions subserved by regions in each cluster. Functional decoding was accomplished by averaging meta-analytic map z-scores across all regions in a cluster for each of the 123 psychological terms and identifying the 5 terms with the highest scores in each cluster. This data-driven approach to functional decoding allows for the mapping of distinct mental concepts and behaviors to cortical territories with distinct profiles of plasticity marker maturation.

Developmental sensitivity analyses

We conducted sensitivity analyses to ensure that our primary developmental findings applied across sexes and were not being driven by potential confounding factors, including individual differences in cortical thickness, cortical gyrification, structural data quality, and cortical partial volume effects. For each sensitivity analysis, the main depth-specific developmental GAMMs were refit while including an additional linear covariate. As in the main analyses, sensitivity GAMMs were used to determine the significance of the developmental effect (FDR corrected), to visualize R1 developmental trajectories, and to quantify the average rate of R1 change and the age of R1 maturation. The clustering analysis based on depth-wise curvature profiles was also repeated using the age splines produced by sensitivity GAMMs.

The first sensitivity analysis included sex as a covariate in GAMMs. Including sex as a covariate allowed us to examine both whether R1 significantly different between sexes, and whether our main developmental findings differed when covarying for participant sex. In addition to models that included a main effect of sex, we fit GAMMs with an age-by-sex interaction term, modeled by an ordered factor-smooth interaction, to test whether R1 developmental splines significantly differed between individuals assigned male and female at birth. The second sensitivity analysis included regional cortical thickness as a covariate to ensure that our R1 results were not attributable to age-related decreases in cortical thickness. The third sensitivity analysis included regional mean curvature as a covariate, which indexes the magnitude of folding present on the cortical surface and thus summarizes gyral and sulcal patterns[111]. This analysis aimed to mitigate any potential effects of inter-individual differences in curvature on our findings, given prior findings that R1 and local curvature are correlated at middle cortical depths[46]. Cortical thickness and mean curvature were both calculated as part of the FreeSurfer longitudinal processing stream and averaged in each HCP-MMP region for each longitudinal imaging session. The fourth sensitivity analysis included FreeSurfer's euler number (averaged across hemispheres) as a covariate to rule out the possibility that age-dependent differences in the quality of cortical surface reconstruction explained our results. The euler number summarizes the topological complexity of reconstructed surfaces (calculated from the number of surface holes) and provides a reliable, quantitative metric of structural image quality[112]. The fifth and final sensitivity analysis included depth-specific measures of the cortex volume fraction in each region as a covariate. This analysis was undertaken to ensure that developmental findings were not impacted by differences in partial volume effects across scans.

Associations with EEG aperiodic activity

EEG data collected from the same accelerated longitudinal sample of participants were integrated with cortical R1 mapping to provide insight into associations between cortical myelin content and local circuit activity. We analyzed four minutes of eyes-open resting state EEG and used this data to isolate the aperiodic component of EEG activity. Aperiodic activity represents "background", population neural activity that occurs independently of band-specific oscillations. Following preprocessing and quality control of EEG measures of aperiodic activity, both EEG and R1

data were available from 128 participants (194 matched longitudinal sessions) of the primary study sample of N = 140.

EEG processing

The EEG data incorporated in this study were preprocessed with EEGLAB version 2022.1[113] and analyzed with the Fitting Oscillations and One Over F (FOOOF)[114] python toolbox as part of a previously published study of aperiodic activity[61]. Detailed information on EEG data acquisition, preprocessing, and analysis with FOOOF is available in McKeon et al.[61]. High-impedance EEG data were acquired using a Biosemi ActiveTwo 64-channel EEG system with a custom electrode cap configuration. Data were resampled to 150 Hz and preprocessed using a revised EEGLAB processing pipeline that included the removal of flatline channels, low frequency drifts, noisy channels, short spontaneous bursts, and incomplete segments of data. Following initial preprocessing, independent component analysis was performed to identify eye-blink artifacts and remove their contribution to the signal. A power spectral density (PSD) was then calculated independently for each electrode by applying Welch's method to preprocessed data (2 second Hamming window; 50% overlap).

Subsequent to fitting electrode-specific PSDs, the FOOOF algorithm (version 1.0.0; later versions known as specparam) was used to separate the aperiodic component from the periodic component (oscillatory peaks) of the PSD. The aperiodic component was extracted from the 1-50 Hz frequency range of each PSD using the following parameters: aperiodic model = fixed, peak width limits = [0.5, 12], mid peak height = 0, peak threshold = 2, max number of peaks = 4. Two measures were then estimated from the fit model of aperiodic activity, including the aperiodic offset (the y-intercept of the aperiodic component) and the aperiodic exponent (the slope of the aperiodic component).

Quality assurance steps were undertaken to ensure that we only analyzed high-quality estimates of aperiodic activity. First, we examined the R^2 and error of each electrode's FOOOF model fit for each longitudinal EEG session. Individual electrodes with low R^2 values (< 0.5) or high spectral fit errors (> 0.1) were excluded from analysis for that session. Given that model fits were generally excellent with a mean R^2 of 0.98 ($\pm$ 0.05) and mean error of 0.04 ($\pm$ 0.02), this step removed data from < 1% of electrodes across all EEG sessions. Next, in accordance with our prior work on the development of aperiodic activity[61], within-session electrode outliers for exponent and offset were identified at the participant level and excluded from analysis. Outliers (< 4.5% of electrodes across all EEG sessions) were classified as single electrodes with a value larger than $\pm$ 2 standard deviations from the session's 64-channel mean. Finally, as in the R1 analysis, we excluded entire EEG sessions where the mean exponent or offset across all 64 channels was greater than $\pm$ 4 standard deviations from the group-level mean of eligible data, resulting in the removal of 4 EEG sessions from analysis. Following data curation, we averaged aperiodic exponent and offset values across left and right EEG electrodes within four frontal cortical territories, guided by a surface-based atlas of EEG electrode positions (described below). Averaging across high-quality electrodes that measure neural signal from the same cortical territory for EEG analysis has dual benefits of enhancing SNR and facilitating anatomical interpretation.

Atlas of EEG electrode positions

Relating cortical R1 to EEG aperiodic activity requires that R1 be quantified in cortical locations proximal to EEG electrodes. This necessitates a mapping of individual electrode locations to individual positions in the cortex. To accomplish such a mapping, we made a surface-based atlas of EEG electrode positions and quantified depth-specific R1 in this custom atlas. EEG electrode positions were first projected from the scalp to the brain's surface in volumetric space using source estimation tools in Brainstorm version 03[115]. The Cartesian coordinates of all electrodes on the 64-channel EEG cap were imported into Brainstorm, localized on the scalp of a generic head model, and projected onto the cortex surface of the MNI152 template, resulting in MNI space centroid coordinates of the most likely cortical location underneath each electrode. Volumetric labels were generated for each

frontal electrode by creating spherical regions of interest around centroid coordinates. Labels were then projected from MNI space to the fsaverage surface using neuromaps. Once represented on the fsaverage surface, electrode labels were dilated to increase surface coverage while preventing nearby labels from overlapping; dilation in the 2D surface prevents labels from encroaching into white matter or distant cortical locations (i.e. gyral hopping)[116]. This mapping procedure resulted in a final reference atlas of frontal cortex EEG electrode positions in a common surface template.

Mirroring the analysis applied with the HCP-MMP atlas, the final EEG electrode atlas was transformed from the fsaverage template to participants' timepoint-specific cortical surfaces to allow for the quantification of R1 in atlas electrode labels. R1 was calculated within superficial depths (depths 1-3) and deep depths (depths 4-7) of each electrode label to relate both superficial and deep cortex R1 to aperiodic activity. As a final step, both R1 and aperiodic activity were averaged bilaterally across groups of electrodes that fell within the ventrolateral prefrontal cortex, the dorsolateral prefrontal cortex, the superior prefrontal cortex, and the primary motor cortex. The assignment of individual electrodes to these broader cortical territories was enabled by the EEG electrode atlas, which transforms conventional depictions of the relative spatial location of electrodes on a 2D circle to the 3D anatomy of the cortex.

In addition to using this surface-based atlas of EEG electrode positions to quantify R1 within the cortex nearest EEG channel locations, a sensitivity analysis was performed using a mapping of electrodes to Brodmann areas that was derived in prior work. Scrivener and Reader[117] localized electrodes to Brodmann areas by visualizing electrode gel artifacts on structural brain images that were acquired during simultaneous EEG and MRI. We applied their Brodmann electrode assignments to our EEG cap to utilize an alternative approach for relating EEG electrodes to cortical areas. We averaged the aperiodic exponent across all electrodes assigned to the same Brodmann area. To relate these data to R1, we quantified superficial and deep R1 within Brodmann areas delineated by the PALS-B12 Brodmann atlas[118]. This sensitivity analysis allowed us to assess convergence of findings across methodologically distinct approaches to EEG channel anatomical localization.

Modeling R1 associations with EEG

We used GAMMs to study age-related changes in aperiodic activity, following the exact model specification described for R1 development GAMMs above. In addition, we extended R1 developmental GAMMs to study relationships between intracortical R1 and EEG-derived measures of aperiodic activity while controlling for age. Primary analyses examined the aperiodic exponent; the aperiodic offset was studied for specificity. GAMMs were fit separately for the four frontal cortical territories (ventrolateral prefrontal cortex, dorsolateral prefrontal cortex, superior prefrontal cortex, primary motor cortex). To first relate aperiodic measures to R1 within superficial and deep cortex independently, we averaged R1 in superficial (depths 1-3) and deep (depths 4-7) cortical depths. We then leveraged the flexible GAMM framework to fit depth-specific GAMMs with (superficial or deep) R1 as the dependent variable, age as a smooth term, aperiodic activity (exponent or offset) as a smooth term, and a random intercept per participant. This model specification allowed us to characterize relationships between R1 and EEG measures across the entire age range studied while controlling for developmental effects. We set the maximum basis complexity of the aperiodic smooth term to 3, given that we did not expect R1-aperiodic relationships to largely deviate from linearity. To determine the relative strength and the significance of the R1-aperiodic relationship in superficial and deep cortex, we extracted the *F*-statistic and the *p*-value associated with the aperiodic smooth term.

Results from the depth-specific models relating EEG to R1 suggested that associations of the aperiodic exponent with R1 may be larger for R1 in deep than in superficial cortex. To formally test for differences in the strength of the R1-aperiodic exponent relationship by depth, we fit GAMMs with a depth interaction term separately for each of the four frontal cortical territories. These models included superficial and deep R1 as the dependent variable, age as a smooth term, and an ordered factor-smooth interaction between depth and the aperiodic exponent. Depth was additionally included as a linear covariate in these models along with a random intercept per participant. The factor smooth

interaction included in this model tests whether the relationship between R1 and the aperiodic exponent significantly differs in magnitude between superficial and deep cortical depths. The same models described above were additionally used in the sensitivity analysis that mapped EEG activity to cortical R1 using Brodmann areas.

Associations with cognitive performance

In addition to participating in MRI and EEG, study participants completed a set of developmentally-sensitive cognitive tasks. Given our prediction that myelination impacts learning and processing efficiency during prefrontal cortex-dependent tasks, we primarily studied performance on a two-stage sequential decision-making task[69,70]; this task was used to derive estimates of learning rates and processing speed. We additionally analyzed data from two eye movement (i.e., saccade) tasks, the anti-saccade and the visually-guided saccade, to test for differential relationships of prefrontal myelin with cognitive versus visuo-motor processing speed. Cognitive data were available from 131 participants (195 matched longitudinal sessions) of the original N = 140 for the two-stage sequential decision-making task and for 125 participants (187 matched longitudinal sessions) for the two saccade tasks.

Cognitive tasks

The two-stage sequential decision-making task[69] asks participants to make a series of choices to earn rewards while they learn about stochastically changing reward contingencies. Specifically, participants make a binary choice in each stage of a two-stage trial and probabilistically receive a reward in the second stage. Participants aim to maximize rewards over 200 task trials delivered in 3 blocks. The first stage of each trial is characterized by fixed action-outcome relationships and the second stage by dynamically changing action-reward probabilities. In our developmentally-validated version of the sequential decision-making task[70], individuals try to maximize “space treasure” rewards by first choosing between two spaceships to visit different planets (stage 1) and next choosing between two aliens on a planet (stage 2). More explicitly, during stage 1 of each trial, individuals choose between one of two spaceships. Both spaceships can take them to the same two planets, but they do so with differing probabilities. Spaceship 1 has a 70% chance of traveling to planet 1 and a 30% chance of traveling to planet 2; spaceship 2 has the inverse probability (30% for planet 1 and 70% for planet 2). These action-outcome probabilities are fixed (i.e., stable) throughout the task. During stage 2 of each trial, individuals choose between one of two aliens present on the planet they arrived at. They may or may not be rewarded with space treasure from the alien. The probability that they are rewarded by each alien slowly and independently drifts via a random walk over the course of the task. Critically, these shifting action-reward probabilities during stage 2 require continued learning of changing contingencies. Together, this two-stage design requires participants to build a stable understanding of the general task structure while simultaneously dynamically updating their understanding of shifting reward probabilities. Prior work has validated that individuals as young as 8 years old learn the task structure, the transition structure (i.e., which spaceship travels to which planet most frequently), and accrue rewards non-randomly[70].

The anti-saccade and visually-guided saccade tasks ask participants to make eye movements away from (anti-saccade) or towards (visually-guided saccade) peripherally presented stimuli. These two tasks require, respectively, the intentional inhibition versus engagement of a reflexive, automatic saccade response. The acquisition and scoring of the anti-saccade[119] and visually-guided saccade[61] tasks are described extensively in published literature from our group. Participants completed 48 trials of the anti-saccade task during which eye tracking was performed with a long-range optics eye-tracking system from Applied Science Laboratories (Model 6000) with a sampling rate of 60 Hz. Nine-point calibrations were performed at the beginning of the eye tracking session. During each of the 48 trials, a red fixation cross was presented at the center of a black screen for a variable time between 500 and 6000 ms, followed by a 200 ms black screen. A yellow cue dot then appeared for 1000 ms pseudo-randomly in one of four positions on the horizontal meridian (2%, 33%, 66%, or 98% of screen

width). Participants were instructed to direct their gaze away from the yellow cue to its horizontal mirror location, i.e., to refrain from looking at the cue and instead saccade to the opposite side of the screen. The visually-guided saccade task was acquired independently of the anti-saccade over 3 runs of 2 trials (60 trials total). Each trial began with a fixation cross presented for 1000 ms, after which a peripheral cue was presented at an unknown location along the horizontal midline. Participants were instructed to saccade to the cue and maintain fixation until the cue disappeared. Eye tracking in the visually-guided saccade task used horizontal electrooculogram channels recorded from facial muscles that were calibrated to eye position along the screen's horizontal meridian.

Learning rates

We used the two-stage sequential decision-making task to derive measures of learning rate. Given that the two stages of the task are designed to require different levels of dynamic learning, we computed learning rates for stages 1 and 2 of the task separately. To operationalize learning rates, we used the hBayesDM package[120] in R to fit a hierarchical Bayesian reinforcement learning model to trial-level task data from all participants. Reinforcement learning models are computational models that parameterize latent neurocognitive processes based on participants' decisions in a task. Hierarchical Bayesian analysis, which estimates both group-level and individual-level parameter estimates (e.g., learning rates) simultaneously, is considered the gold-standard approach to model parameterization[120–123]. The hierarchical Bayesian approach uses group-level population distributions of parameters as priors when estimating individual-level parameters, which produces more robust and stable estimates of model parameters per person, thereby enabling better individual inference[120–122]. Posterior inference in the hBayesDM model was conducted using the No-U-Turn Sampler (NUTS), which is a part of the Hamiltonian Monte Carlo framework for Markov chain Monte Carlo (MCMC) sampling. The model was fit with 4 chains, each running for a total of 4,000 iterations, which included 1,000 warmup samples for each chain. Hyperparameters consisted of a population-level mean and standard deviation. Individual-level parameters were assigned weakly informative priors, which help regularize the estimates and ensure that the individual-level parameters are not overly constrained.

The hBayesDM reinforcement learning model analyzed in this work is a 7-parameter model fit identically as in our prior study that used the same sequential decision-making task in a similar adolescent and young adult sample[124]. The model comes pre-programmed with the hBayesDM package based on the widely adopted reinforcement learning model originally applied by Daw et al.[69] to this same task. The 7 model parameters include stage 1 and stage 2 learning rates (α_1 and α_2), stage 1 and stage 2 inverse temperature (β_1 and β_2), a perseverance parameter (π), a model-based weight (w), and an eligibility trace (λ). These parameters have been described extensively in prior studies[69,125]. The learning rate parameter analyzed here captures how quickly an individual updates their expectations and choices based on new information (namely, recent outcomes in the task). Higher learning rates are indicative of greater sensitivity to more recent information and faster updating, and thus a faster step size or speed of learning[123]. Of note, after fitting the 7-parameter model, we confirmed that it had better performance than alternative model formulations with 6 parameters only (identical to the 7-parameter model, but without the eligibility trace) and 4 parameters only (across-stage learning rate, across-stage inverse temperature, perseverance, and model-based weight). Better performance was indicated by a lower Leave-One-Out Information Criterion (LOOIC) and Widely Applicable Information Criterion (WAIC).

Processing speed

Response times during cognitive tasks were used as readouts of processing speed. Given that the two-stage sequential decision-making task and the anti-saccade task require decision making and response inhibition respectively, response times on these tasks index the speed of processing when endogenously employing higher-order executive functions. In contrast, the visually-guided saccade task only requires simple, reflexive foveation of a stimulus; response times on this task thus reflect exogenously-driven sensorimotor processing. For the sequential decision-making task, average

response times were calculated for stage 1 and stage 2 of the task independently as each stage requires making a decision based on different information[70]. Response time on this task is the time it takes for participants to make a binary choice through a keyboard press following presentation of task stimuli.

For the anti-saccade task, response time was calculated as the average latency to initiate a saccade on correct trials of the task. We only considered correct trials so as to only analyze timepoints where higher-order inhibitory control over reflexive responding was engaged successfully. Correct trials are defined as those in which the first eye movement during the saccade epoch with a velocity greater than or equal to 30◦/sec is made to the mirror location (opposite in direction) from the peripheral cue. Consistent with established protocol, we excluded trials with eye blinks as well as trials with response latencies less than 100 ms (express saccades) or greater than 1000 ms (non-response). For the visually-guided saccade task, response time was calculated as the average latency to initiate a saccade on all trials of the task while again excluding trials with response latencies less than 100 ms or greater than 1000 ms as well as trials with position errors greater than 23 degrees.

Modeling R1 associations with cognition

The primary set of cognitive analyses examined stage-specific learning rates and processing speeds from the two-stage sequential decision-making task. To first offer insight into whether learning rates and processing speeds systematically differed between the two stages of the task, we implemented two-sided paired samples t-tests. Next, to provide developmental context, we adopted the model specification described for R1 development GAMMs to independently study developmental changes in all four task measures. Finally, for analyses relating sequential decision-making task measures to cortical R1, we followed the same modeling procedure described above for EEG. We began by independently examining relationships between cognitive measures and R1 averaged within superficial cortical depths (1-3) and deep cortical depths (4-7) of each HCP-MMP frontal region. Depth-specific GAMMs were run with superficial or deep R1 as the dependent variable, age as a smooth term, the cognitive measure (learning rate or processing speed) as a smooth term, and a random intercept per participant. These GAMMs provided initial evidence for significant relationships between sequential decision-making task measures and R1 in deep and in superficial cortex. To test whether the strength of these relationships significantly differed between deep and superficial cortex, we used an ordered factor-smooth interaction in GAMMs between depth and the cognitive measure (as above with EEG) while including depth as a linear covariate.

Depth interaction models provided no evidence for significant differences in the strength of the relationship between sequential decision-making task measures and R1 in superficial and deep cortex. We therefore amended GAMMs to fit final models with a global cognitive smooth that captured the relationship between sequential decision-making task measures and R1 in both deep and superficial cortex. These “combined-depth” GAMMs were used for statistical inference and included superficial and deep R1 as the dependent variable, a smooth term for age, a smooth term for the cognitive measure, a linear effect of depth, and random intercepts. After fitting combined-depth GAMMs for sequential decision-making task measures, we additionally fit them with anti-saccade and visually-guided saccade response times for cognitive specificity analyses. As in the developmental analyses, the false discovery rate correction was applied to correct *p*-values across frontal lobe regions (p_{FDR}) to control for multiple comparisons.

Functional decoding of learning rate-linked regions

Associations between cortical R1 and learning rates (stage 2) showed a considerable degree of anatomical specificity. To determine the primary psychological functions ascribed to prefrontal regions wherein higher R1 was associated with a faster learning rate, we performed Neurosynth-based functional decoding with the set of 123 meta-analytic term maps. We averaged meta-analytic map z-

scores across all frontal regions with a significant learning rate association and identified terms with the highest scores, providing an empirically-derived functional characterization.

Data availability

Raw neuroimaging data from this study is available upon request. This study incorporated previously published cortical data, including the S-A axis (accessed in fslr 32k space from https://github.com/PennLINC/S-A_ArchetypalAxis), a myelin water fraction map (provided in MNI space at https://sourceforge.net/projects/myelin-water-atlas/), left hemisphere myelin basic protein gene expression values (released in fslr 32k space through https://github.com/kwagstyl/MAGICC), and a histological axis of cytoarchitectural variation (Hist-G2 obtainable in fslr 32k space from https://bigbrainwarp.readthedocs.io/en/latest/pages/toolbox_contents.html). It additionally used Neurosynth version 0.7 data, released on github (https://github.com/neurosynth/neurosynth-data), and volumetric and surface templates made available through TemplateFlow (https://www.templateflow.org/).

Code availability

All original code generated for this study is available on github at https://github.com/LabNeuroCogDevel/corticalmyelin_maturation. In addition, a detailed guide to code implementation describing all analytic steps and statistical analyses is provided along with the github repository at https://labneurocogdevel.github.io/corticalmyelin_maturation. Original study code integrated publicly available software. MRI processing utilized a containerized version of the SPM BIDS app (available at https://hub.docker.com/r/bids/spm/), a containerized FreeSurfer BIDS app (available at https://hub.docker.com/r/bids/freesurfer; tag freesurfer:7.4.1-202309), a Neuromaps container (available at https://hub.docker.com/r/netneurolab/neuromaps; tag 0.0.4), AFNI (available at https://afni.nimh.nih.gov/pub/dist/doc/htmldoc/index.html; version 23.1.10), and Connectome workbench (available at https://github.com/Washington-University/workbench/releases; version 1.5.0). EEG processing used EEGLab (available at https://eeglab.org/download/; version 2022.1), FOOOF (available at https://fooof-tools.github.io/fooof/; version 1.0.0), and Brainstorm 03 (available at https://github.com/brainstorm-tools/brainstorm3). Neurosynth analyses relied on NIMARE (available at https://nimare.readthedocs.io/en/latest/installation.html). Spatial autocorrelation preserving nulls were generated with BrainSMASH version 0.11.0 (https://brainsmash.readthedocs.io/en/latest/index.html). Reinforcement learning models were fit with hierarchical Bayesian modeling with the model specified under “Two-Step Task – Hybrid Model, with 7 parameters (original model)” in hBayesDM (https://hbayesdm.readthedocs.io/en/develop/models.html). All statistical analyses were conducted in R version 4.2.3 (https://cran.r-project.org/bin/macosx/).

Acknowledgements

This work was supported by the National Institutes of Health (NIH), including T32MH016804 to VJS, T32AA007453 to DP, F31MH132246 to SDM, and R01MH067924 to BL. Additional funding was provided by the Staunton Farm Foundation. This work used Bridges-2 at Pittsburgh Supercomputing Center through allocation soc23000rp from the Advanced Cyberinfrastructure Coordination Ecosystem: Services & Support (ACCESS) program, which is supported by National Science Foundation grants #2138259, #2138286, #2138307, #2137603, and #2138296.

We are grateful to personnel at the Magnetic Resonance Research Center (MRRC) at UPMC Presbyterian, especially Chan Moon and Hoby Hetherington, for their valuable assistance in planning, implementing, and performing the 7T imaging acquisitions. We also thank the University of Pittsburgh Clinical and Translational Science Institute (CTSI) for their support in recruiting participants, as well as their support by the NIH through UL1TR001857.

Author Contributions

VJS designed the study with support from FJC and BL. AF acquired the neuroimaging data under the supervision of FJC and BL and using resources acquired by BL. VJS curated and quality controlled the MRI data with support from WF. VJS developed and implemented the MP2RAGE processing pipeline. SDM processed the EEG data. DP analyzed the two-stage sequential decision-making task data. SDM and WF analyzed data from the two saccade tasks. VJS carried out all statistical analyses with guidance from FJC. VJS wrote all study-specific code and created all figures. VJS wrote the original manuscript. All authors reviewed and revised the manuscript. FJC and BL provided scientific mentorship throughout the lifecycle of the project.

Competing Interests

The authors declare no competing interests.

Materials and Correspondence

Please address all requests for materials to the corresponding authors Valerie J. Sydnor and Beatriz Luna.

References

1. Donahue, C. J., Glasser, M. F., Preuss, T. M., Rilling, J. K. & Essen, D. C. V. Quantitative assessment of prefrontal cortex in humans relative to nonhuman primates. *PNAS* **115**, E5183–E5192 (2018).
2. Buckner, R. L. & Krienen, F. M. The evolution of distributed association networks in the human brain. *Trends Cogn Sci* **17**, 648–665 (2013).
3. Sydnor, V. J. *et al.* Neurodevelopment of the association cortices: Patterns, mechanisms, and implications for psychopathology. *Neuron* **109**, 2820–2846 (2021).
4. Larsen, B. & Luna, B. Adolescence as a neurobiological critical period for the development of higher-order cognition. *Neurosci Biobehav Rev* **94**, 179–195 (2018).
5. Sydnor, V. J. *et al.* Intrinsic activity development unfolds along a sensorimotor–association cortical axis in youth. *Nat Neurosci* **26**, 638–649 (2023).
6. Petanjek, Z. *et al.* Extraordinary neoteny of synaptic spines in the human prefrontal cortex. *Proc Natl Acad Sci U S A* **108**, 13281–13286 (2011).
7. Gogtay, N. *et al.* Dynamic mapping of human cortical development during childhood through early adulthood. *PNAS* **101**, 8174–8179 (2004).
8. Zhang, S. *et al.* In vivo whole-cortex marker of excitation-inhibition ratio indexes cortical maturation and cognitive ability in youth. *Proceedings of the National Academy of Sciences* **121**, e2318641121 (2024).
9. Larsen, B., Sydnor, V. J., Keller, A. S., Yeo, B. T. T. & Satterthwaite, T. D. A critical period plasticity framework for the sensorimotor–association axis of cortical neurodevelopment. *Trends in Neurosciences* **46**, 847–862 (2023).
10. Burman, K. J., Lui, L. L., Rosa, M. G. P. & Bourne, J. A. Development of non-phosphorylated neurofilament protein expression in neurones of the New World monkey dorsolateral frontal cortex. *European Journal of Neuroscience* **25**, 1767–1779 (2007).
11. Paquola, C. *et al.* Shifts in myeloarchitecture characterise adolescent development of cortical gradients. *Elife* **8**, e50482 (2019).
12. Baum, G. L. *et al.* Graded Variation in T1w/T2w Ratio during Adolescence: Measurement, Caveats, and Implications for Development of Cortical Myelin. *J. Neurosci.* **42**, 5681–5694 (2022).
13. Grydeland, H. *et al.* Waves of Maturation and Senescence in Micro-structural MRI Markers of Human Cortical Myelination over the Lifespan. *Cereb Cortex* **29**, 1369–1381 (2019).
14. Flechsig Of Leipsic, P. DEVELOPMENTAL (MYELOGENETIC) LOCALISATION OF THE CEREBRAL CORTEX IN THE HUMAN SUBJECT. *The Lancet* **158**, 1027–1030 (1901).
15. García-Cabezas, M. Á., Hacker, J. L. & Zikopoulos, B. A Protocol for Cortical Type Analysis of the Human Neocortex Applied on Histological Samples, the Atlas of Von Economo and Koskinas, and Magnetic Resonance Imaging. *Front. Neuroanat.* **14**, (2020).
16. Douglas, R. J. & Martin, K. A. C. NEURONAL CIRCUITS OF THE NEOCORTEX. *Annual Review of Neuroscience* **27**, 419–451 (2004).
17. Hutsler, J. J., Lee, D.-G. & Porter, K. K. Comparative analysis of cortical layering and supragranular layer enlargement in rodent carnivore and primate species. *Brain Research* **1052**, 71–81 (2005).
18. Alizadeh, A., Englitz, B. & Zeldenrust, F. How the layer-dependent ratio of excitatory to inhibitory cells shapes cortical coding in balanced networks. 2024.11.28.625852 Preprint at https://doi.org/10.1101/2024.11.28.625852 (2024).
19. Galakhova, A. A. *et al.* Evolution of cortical neurons supporting human cognition. *Trends in Cognitive Sciences* **26**, 909–922 (2022).
20. Rolls, E. T. & Mills, W. P. C. Computations in the deep vs superficial layers of the cerebral cortex. *Neurobiol Learn Mem* **145**, 205–221 (2017).

21. Xin, W. *et al.* Oligodendrocytes and myelin limit neuronal plasticity in visual cortex. *Nature* **633**, 856–863 (2024).
22. McGee, A. W., Yang, Y., Fischer, Q. S., Daw, N. W. & Strittmatter, S. M. Experience-Driven Plasticity of Visual Cortex Limited by Myelin and Nogo Receptor. *Science* **309**, 2222–2226 (2005).
23. Takesian, A. E. & Hensch, T. K. Chapter 1 - Balancing Plasticity/Stability Across Brain Development. in *Progress in Brain Research* (eds. Merzenich, M. M., Nahum, M. & Van Vleet, T. M.) vol. 207 3–34 (Elsevier, 2013).
24. Call, C. L. & Bergles, D. E. Cortical neurons exhibit diverse myelination patterns that scale between mouse brain regions and regenerate after demyelination. *Nat Commun* **12**, 4767 (2021).
25. Stedehouder, J. *et al.* Fast-spiking Parvalbumin Interneurons are Frequently Myelinated in the Cerebral Cortex of Mice and Humans. *Cerebral Cortex* **27**, 5001–5013 (2017).
26. Micheva, K. D. *et al.* A large fraction of neocortical myelin ensheathes axons of local inhibitory neurons. *eLife* **5**, e15784 (2016).
27. Fagiolini, M. & Hensch, T. K. Inhibitory threshold for critical-period activation in primary visual cortex. *Nature* **404**, 183–186 (2000).
28. Reh, R. K. *et al.* Critical period regulation across multiple timescales. *Proc Natl Acad Sci U S A* **117**, 23242–23251 (2020).
29. Filbin, M. T. Myelin-associated inhibitors of axonal regeneration in the adult mammalian CNS. *Nat Rev Neurosci* **4**, 703–713 (2003).
30. Chen, M. S. *et al.* Nogo-A is a myelin-associated neurite outgrowth inhibitor and an antigen for monoclonal antibody IN-1. *Nature* **403**, 434–439 (2000).
31. Zemmar, A. *et al.* Oligodendrocyte- and Neuron-Specific Nogo-A Restrict Dendritic Branching and Spine Density in the Adult Mouse Motor Cortex. *Cereb Cortex* **28**, 2109–2117 (2018).
32. Raiker, S. J. *et al.* Oligodendrocyte-Myelin Glycoprotein and Nogo Negatively Regulate Activity-Dependent Synaptic Plasticity. *J Neurosci* **30**, 12432–12445 (2010).
33. de Faria, O. *et al.* Periods of synchronized myelin changes shape brain function and plasticity. *Nat Neurosci* **24**, 1508–1521 (2021).
34. Hughes, E. G., Orthmann-Murphy, J. L., Langseth, A. J. & Bergles, D. E. Myelin remodeling through experience-dependent oligodendrogenesis in the adult somatosensory cortex. *Nat Neurosci* **21**, 696–706 (2018).
35. Hill, R. A., Li, A. M. & Grutzendler, J. Lifelong cortical myelin plasticity and age-related degeneration in the live mammalian brain. *Nat Neurosci* **21**, 683–695 (2018).
36. Xin, W. & Chan, J. R. Myelin plasticity: sculpting circuits in learning and memory. *Nat Rev Neurosci* **21**, 682–694 (2020).
37. Bacmeister, C. M. *et al.* Motor Learning Drives Dynamic Patterns of Intermittent Myelination on Learning-activated Axons. *Nat Neurosci* **25**, 1300–1313 (2022).
38. Shimizu, T. *et al.* Oligodendrocyte dynamics dictate cognitive performance outcomes of working memory training in mice. *Nat Commun* **14**, 6499 (2023).
39. McKenzie, I. A. *et al.* Motor skill learning requires active central myelination. *Science* **346**, 318–322 (2014).
40. Pan, S., Mayoral, S. R., Choi, H. S., Chan, J. R. & Kheirbek, M. A. Preservation of a remote fear memory requires new myelin formation. *Nat Neurosci* **23**, 487–499 (2020).
41. Hettwer, M. D. *et al.* Longitudinal variation in resilient psychosocial functioning is associated with ongoing cortical myelination and functional reorganization during adolescence. *Nat Commun* **15**, 6283 (2024).
42. Shafee, R., Buckner, R. L. & Fischl, B. Gray matter myelination of 1555 human brains using partial volume corrected MRI images. *Neuroimage* **105**, 473–485 (2015).
43. Whitaker, K. J. *et al.* Adolescence is associated with genomically patterned consolidation of the hubs of the human brain connectome. *Proc Natl Acad Sci U S A* **113**, 9105–9110 (2016).

44. Bock, N. A., Kocharyan, A., Liu, J. V. & Silva, A. C. Visualizing the entire cortical myelination pattern in marmosets with magnetic resonance imaging. *J Neurosci Methods* **185**, 15–22 (2009).
45. Tardif, C. L., Bedell, B. J., Eskildsen, S. F., Collins, D. L. & Pike, G. B. Quantitative magnetic resonance imaging of cortical multiple sclerosis pathology. *Mult Scler Int* **2012**, 742018 (2012).
46. Sereno, M. I., Lutti, A., Weiskopf, N. & Dick, F. Mapping the Human Cortical Surface by Combining Quantitative T1 with Retinotopy. *Cereb Cortex* **23**, 2261–2268 (2013).
47. Lutti, A., Dick, F., Sereno, M. I. & Weiskopf, N. Using high-resolution quantitative mapping of R1 as an index of cortical myelination. *NeuroImage* **93**, 176–188 (2014).
48. Haast, R. A. M., Ivanov, D., Formisano, E. & Uludağ, K. Reproducibility and Reliability of Quantitative and Weighted T1 and T2∗ Mapping for Myelin-Based Cortical Parcellation at 7 Tesla. *Frontiers in Neuroanatomy* **10**, (2016).
49. Benamer, N., Vidal, M., Balia, M. & Angulo, M. C. Myelination of parvalbumin interneurons shapes the function of cortical sensory inhibitory circuits. *Nat Commun* **11**, 5151 (2020).
50. Lazari, A. *et al.* A macroscopic link between interhemispheric tract myelination and cortico-cortical interactions during action reprogramming. *Nat Commun* **13**, 4253 (2022).
51. Waxman, S. G. Determinants of conduction velocity in myelinated nerve fibers. *Muscle Nerve* **3**, 141–150 (1980).
52. García-Cabezas, M. Á., Joyce, M. K. P., John, Y. J., Zikopoulos, B. & Barbas, H. Mirror trends of plasticity and stability indicators in primate prefrontal cortex. *Eur. J. Neurosci.* **46**, 2392–2405 (2017).
53. Paquola, C. & Hong, S.-J. The Potential of Myelin-Sensitive Imaging: Redefining Spatiotemporal Patterns of Myeloarchitecture. *Biol Psychiatry* **93**, 442–454 (2023).
54. Palomero-Gallagher, N. & Zilles, K. Cortical layers: Cyto-, myelo-, receptor- and synaptic architecture in human cortical areas. *NeuroImage* **197**, 716–741 (2019).
55. Wagstyl, K. *et al.* Transcriptional Cartography Integrates Multiscale Biology of the Human Cortex. *eLife* **12**, (2024).
56. Liu, H. *et al.* Myelin Water Atlas: A Template for Myelin Distribution in the Brain. *Journal of Neuroimaging* **29**, 699–706 (2019).
57. Flechsig, P. E. *Anatomie des menschlichen Gehirns und Rückenmarks auf myelogenetischer Grundlage*. (G. Thieme, 1920).
58. Paquola, C. *et al.* The BigBrainWarp toolbox for integration of BigBrain 3D histology with multimodal neuroimaging. *eLife* **10**, e70119 (2021).
59. Tomassy, G. S. *et al.* Distinct profiles of myelin distribution along single axons of pyramidal neurons in the neocortex. *Science* **344**, 319–324 (2014).
60. Gao, R., Peterson, E. J. & Voytek, B. Inferring synaptic excitation/inhibition balance from field potentials. *NeuroImage* **158**, 70–78 (2017).
61. McKeon, S. D. *et al.* Aperiodic EEG and 7T MRSI evidence for maturation of E/I balance supporting the development of working memory through adolescence. *Dev Cogn Neurosci* **66**, 101373 (2024).
62. Gao, R., van den Brink, R. L., Pfeffer, T. & Voytek, B. Neuronal timescales are functionally dynamic and shaped by cortical microarchitecture. *Elife* **9**, e61277 (2020).
63. Halgren, M. *et al.* The timescale and magnitude of 1/f aperiodic activity decrease with cortical depth in humans, macaques, and mice. 2021.07.28.454235 Preprint at https://doi.org/10.1101/2021.07.28.454235 (2021).
64. Hill, A. T., Clark, G. M., Bigelow, F. J., Lum, J. A. G. & Enticott, P. G. Periodic and aperiodic neural activity displays age-dependent changes across early-to-middle childhood. *Developmental Cognitive Neuroscience* **54**, 101076 (2022).
65. Cellier, D., Riddle, J., Petersen, I. & Hwang, K. The development of theta and alpha neural oscillations from ages 3 to 24 years. *Dev Cogn Neurosci* **50**, 100969 (2021).
66. Kirschstein, T. & Köhling, R. What is the Source of the EEG? *Clin EEG Neurosci* **40**, 146–149 (2009).

67. Thio, B. J. & Grill, W. M. Relative contributions of different neural sources to the EEG. *Neuroimage* **275**, 120179 (2023).
68. Manning, J. R., Jacobs, J., Fried, I. & Kahana, M. J. Broadband Shifts in Local Field Potential Power Spectra Are Correlated with Single-Neuron Spiking in Humans. *J. Neurosci.* **29**, 13613–13620 (2009).
69. Daw, N. D., Gershman, S. J., Seymour, B., Dayan, P. & Dolan, R. J. Model-based influences on humans' choices and striatal prediction errors. *Neuron* **69**, 1204–1215 (2011).
70. Decker, J. H., Otto, A. R., Daw, N. D. & Hartley, C. A. From Creatures of Habit to Goal-Directed Learners. *Psychol Sci* **27**, 848–858 (2016).
71. Sur, M. & Leamey, C. A. Development and plasticity of cortical areas and networks. *Nat Rev Neurosci* **2**, 251–262 (2001).
72. Mohan, H. *et al.* Dendritic and Axonal Architecture of Individual Pyramidal Neurons across Layers of Adult Human Neocortex. *Cereb Cortex* **25**, 4839–4853 (2015).
73. Mount, C. & Monje, M. Wrapped to adapt: experience-dependent myelination. *Neuron* **95**, 743–756 (2017).
74. Bechler, M. E., Swire, M. & ffrench-Constant, C. Intrinsic and adaptive myelination—A sequential mechanism for smart wiring in the brain. *Developmental Neurobiology* **78**, 68–79 (2018).
75. Xu, Y. K. T. *et al.* Brain-wide mapping of oligodendrocyte organization and oligodendrogenesis across the murine lifespan. 2024.09.06.611254 Preprint at https://doi.org/10.1101/2024.09.06.611254 (2024).
76. Valk, S. L. *et al.* Functional and microstructural plasticity following social and interoceptive mental training. *Elife* **12**, e85188 (2023).
77. Bercury, K. K. & Macklin, W. B. Dynamics and Mechanisms of CNS Myelination. *Developmental Cell* **32**, 447–458 (2015).
78. Stedehouder, J., Brizee, D., Shpak, G. & Kushner, S. A. Activity-Dependent Myelination of Parvalbumin Interneurons Mediated by Axonal Morphological Plasticity. *J Neurosci* **38**, 3631–3642 (2018).
79. Moissidis, M. *et al.* A postnatal molecular switch drives the activity-dependent maturation of parvalbumin interneurons. 2024.04.08.588555 Preprint at https://doi.org/10.1101/2024.04.08.588555 (2024).
80. Sydnor, V. J. *et al.* A sensorimotor-association axis of thalamocortical connection development. 2024.06.13.598749 Preprint at https://doi.org/10.1101/2024.06.13.598749 (2024).
81. Hill, J. *et al.* Similar patterns of cortical expansion during human development and evolution. *Proc Natl Acad Sci U S A* **107**, 13135–13140 (2010).
82. Xu, T. *et al.* Cross-species functional alignment reveals evolutionary hierarchy within the connectome. *NeuroImage* **223**, 117346 (2020).
83. Voytek, B. *et al.* Age-Related Changes in 1/f Neural Electrophysiological Noise. *J Neurosci* **35**, 13257–13265 (2015).
84. Zhu, J., Hammond, B. M., Zhou, X. M. & Constantinidis, C. Laminar pattern of adolescent development changes in working memory neuronal activity. *Journal of Neurophysiology* **130**, 980–989 (2023).
85. Finn, E. S., Huber, L., Jangraw, D. C., Molfese, P. J. & Bandettini, P. A. Layer-dependent activity in human prefrontal cortex during working memory. *Nat Neurosci* **22**, 1687–1695 (2019).
86. Dinse, J. *et al.* A cytoarchitecture-driven myelin model reveals area-specific signatures in human primary and secondary areas using ultra-high resolution in-vivo brain MRI. *NeuroImage* **114**, 71–87 (2015).
87. Matosin, N. *et al.* Associations of psychiatric disease and aging on FKBP5 expression converge on cortical supragranular neurons. 2021.01.27.428487 Preprint at https://doi.org/10.1101/2021.01.27.428487 (2022).
88. Arnsten, A. F. T. & Datta, D. Characterizing the Most Vulnerable Prefrontal Cortical Neurons in Schizophrenia. *AJP* **181**, 861–864 (2024).

89. Marques, J. P. *et al.* MP2RAGE, a self bias-field corrected sequence for improved segmentation and T1-mapping at high field. *Neuroimage* **49**, 1271–1281 (2010).
90. O'Brien, K. R. *et al.* Robust T1-Weighted Structural Brain Imaging and Morphometry at 7T Using MP2RAGE. *PLOS ONE* **9**, e99676 (2014).
91. Haast, R. A. M. *et al.* Effects of MP2RAGE B1+ sensitivity on inter-site T1 reproducibility and hippocampal morphometry at 7T. *NeuroImage* **224**, 117373 (2021).
92. Oliveira, Í. A. F., Roos, T., Dumoulin, S. O., Siero, J. C. W. & van der Zwaag, W. Can 7T MPRAGE match MP2RAGE for gray-white matter contrast? *Neuroimage* **240**, 118384 (2021).
93. Osetrova, M. *et al.* Lipidome atlas of the adult human brain. *Nat Commun* **15**, 4455 (2024).
94. Lazari, A. & Lipp, I. Can MRI measure myelin? Systematic review, qualitative assessment, and meta-analysis of studies validating microstructural imaging with myelin histology. *Neuroimage* **230**, 117744 (2021).
95. Mancini, M. *et al.* An interactive meta-analysis of MRI biomarkers of myelin. *eLife* **9**, e61523 (2020).
96. Mottershead, J. P. *et al.* High field MRI correlates of myelin content and axonal density in multiple sclerosis--a post-mortem study of the spinal cord. *J Neurol* **250**, 1293–1301 (2003).
97. Weiskopf, N. *et al.* Unified segmentation based correction of R1 brain maps for RF transmit field inhomogeneities (UNICORT). *Neuroimage* **54**, 2116 (2011).
98. Reuter, M., Schmansky, N. J., Rosas, H. D. & Fischl, B. Within-subject template estimation for unbiased longitudinal image analysis. *Neuroimage* **61**, 1402 (2012).
99. Wagstyl, K. *et al.* Mapping Cortical Laminar Structure in the 3D BigBrain. *Cerebral Cortex* **28**, 2551–2562 (2018).
100. Glasser, M. F. *et al.* A multi-modal parcellation of human cerebral cortex. *Nature* **536**, 171–178 (2016).
101. Covitz, S. *et al.* Curation of BIDS (CuBIDS): A workflow and software package for streamlining reproducible curation of large BIDS datasets. *Neuroimage* **263**, 119609 (2022).
102. Yarkoni, T., Poldrack, R. A., Nichols, T. E., Van Essen, D. C. & Wager, T. D. Large-scale automated synthesis of human functional neuroimaging data. *Nat Methods* **8**, 665–670 (2011).
103. Salo, T. *et al.* NiMARE: Neuroimaging Meta-Analysis Research Environment. *Aperture Neuro* **3**, 1–32 (2023).
104. Shafiei, G. *et al.* Topographic gradients of intrinsic dynamics across neocortex. *eLife* **9**, e62116 (2020).
105. Hansen, J. Y. *et al.* Mapping neurotransmitter systems to the structural and functional organization of the human neocortex. *Nat Neurosci* **25**, 1569–1581 (2022).
106. Poldrack, R. *et al.* The Cognitive Atlas: Toward a Knowledge Foundation for Cognitive Neuroscience. *Frontiers in Neuroinformatics* **5**, (2011).
107. Burt, J. B., Helmer, M., Shinn, M., Anticevic, A. & Murray, J. D. Generative modeling of brain maps with spatial autocorrelation. *bioRxiv* 2020.02.18.955054 (2020) doi:10.1101/2020.02.18.955054.
108. Wood, S. N. *Generalized Additive Models: An Introduction with R*. (Chapman and Hall/CRC, New York, 2017). doi:10.1201/9781315370279.
109. Gavin L. Simpson. gratia: Graceful ggplot-Based Graphics and Other Functions for GAMs Fitted using mgcv. https://gavinsimpson.github.io/gratia/ (2022).
110. Charrad, M., Ghazzali, N., Boiteau, V. & Niknafs, A. NbClust: An R Package for Determining the Relevant Number of Clusters in a Data Set. *Journal of Statistical Software* **61**, 1–36 (2014).
111. Luders, E. *et al.* A curvature-based approach to estimate local gyrification on the cortical surface. *NeuroImage* **29**, 1224–1230 (2006).
112. Rosen, A. F. G. *et al.* Quantitative Assessment of Structural Image Quality. *NeuroImage* **169**, 407 (2017).
113. Delorme, A. & Makeig, S. EEGLAB: an open source toolbox for analysis of single-trial EEG dynamics including independent component analysis. *J Neurosci Methods* **134**, 9–21 (2004).

114. Donoghue, T. *et al.* Parameterizing neural power spectra into periodic and aperiodic components. *Nat Neurosci* **23**, 1655–1665 (2020).
115. Tadel, F., Baillet, S., Mosher, J. C., Pantazis, D. & Leahy, R. M. Brainstorm: A User-Friendly Application for MEG/EEG Analysis. *Computational Intelligence and Neuroscience* **2011**, 879716 (2011).
116. Coalson, T. S., Van Essen, D. C. & Glasser, M. F. The impact of traditional neuroimaging methods on the spatial localization of cortical areas. *Proceedings of the National Academy of Sciences* **115**, E6356–E6365 (2018).
117. Scrivener, C. L. & Reader, A. T. Variability of EEG electrode positions and their underlying brain regions: visualizing gel artifacts from a simultaneous EEG-fMRI dataset. *Brain Behav* **12**, e2476 (2022).
118. Van Essen, D. C. A Population-Average, Landmark- and Surface-based (PALS) atlas of human cerebral cortex. *NeuroImage* **28**, 635–662 (2005).
119. Ojha, A., Parr, A. C., Foran, W., Calabro, F. J. & Luna, B. Puberty contributes to adolescent development of fronto-striatal functional connectivity supporting inhibitory control. *Developmental Cognitive Neuroscience* **58**, 101183 (2022).
120. Ahn, W.-Y., Haines, N. & Zhang, L. Revealing Neurocomputational Mechanisms of Reinforcement Learning and Decision-Making With the hBayesDM Package. *Computational Psychiatry (Cambridge, Mass.)* **1**, 24 (2017).
121. van Geen, C. & Gerraty, R. T. Hierarchical Bayesian models of reinforcement learning: Introduction and comparison to alternative methods. *Journal of Mathematical Psychology* **105**, 102602 (2021).
122. Katahira, K. How hierarchical models improve point estimates of model parameters at the individual level. *Journal of Mathematical Psychology* **73**, 37–58 (2016).
123. Zhang, L., Lengersdorff, L., Mikus, N., Gläscher, J. & Lamm, C. Using reinforcement learning models in social neuroscience: frameworks, pitfalls and suggestions of best practices. *Social Cognitive and Affective Neuroscience* **15**, 695 (2020).
124. Petrie, D. J. *et al.* Maturation of striatal dopamine supports the development of habitual behavior through adolescence. 2025.01.06.631527 Preprint at https://doi.org/10.1101/2025.01.06.631527 (2025).
125. Wunderlich, K., Smittenaar, P. & Dolan, R. J. Dopamine Enhances Model-Based over Model-Free Choice Behavior. *Neuron* **75**, 418 (2012).

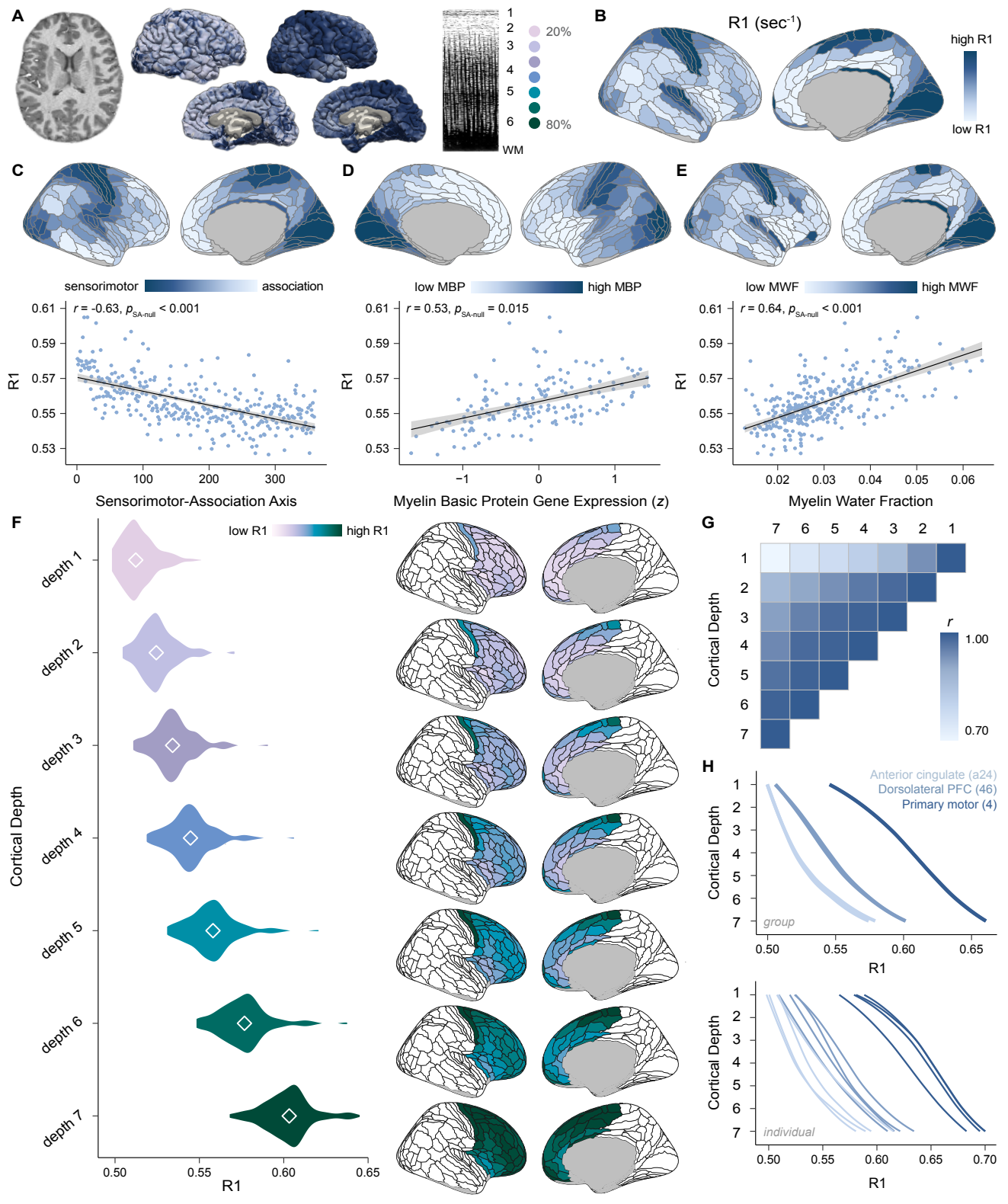
A
1
2
3
4
5
6
WM
20%
80%
B
R1 (sec-1)
high R1
low R1
C
sensorimotor
association
r = -0.63, pSA-null < 0.001
R1
Sensorimotor-Association Axis
D
low MBP
high MBP
r = 0.53, pSA-null = 0.015
Myelin Basic Protein Gene Expression (z)
E
low MWF
high MWF
r = 0.64, pSA-null < 0.001
Myelin Water Fraction
F
low R1
high R1
depth 1
depth 2
depth 3
depth 4
depth 5
depth 6
depth 7
Cortical Depth
R1
G
Cortical Depth
r
1.00
0.70
H
Anterior cingulate (a24)
Dorsolateral PFC (46)
Primary motor (4)
group
individual
Cortical Depth
R1

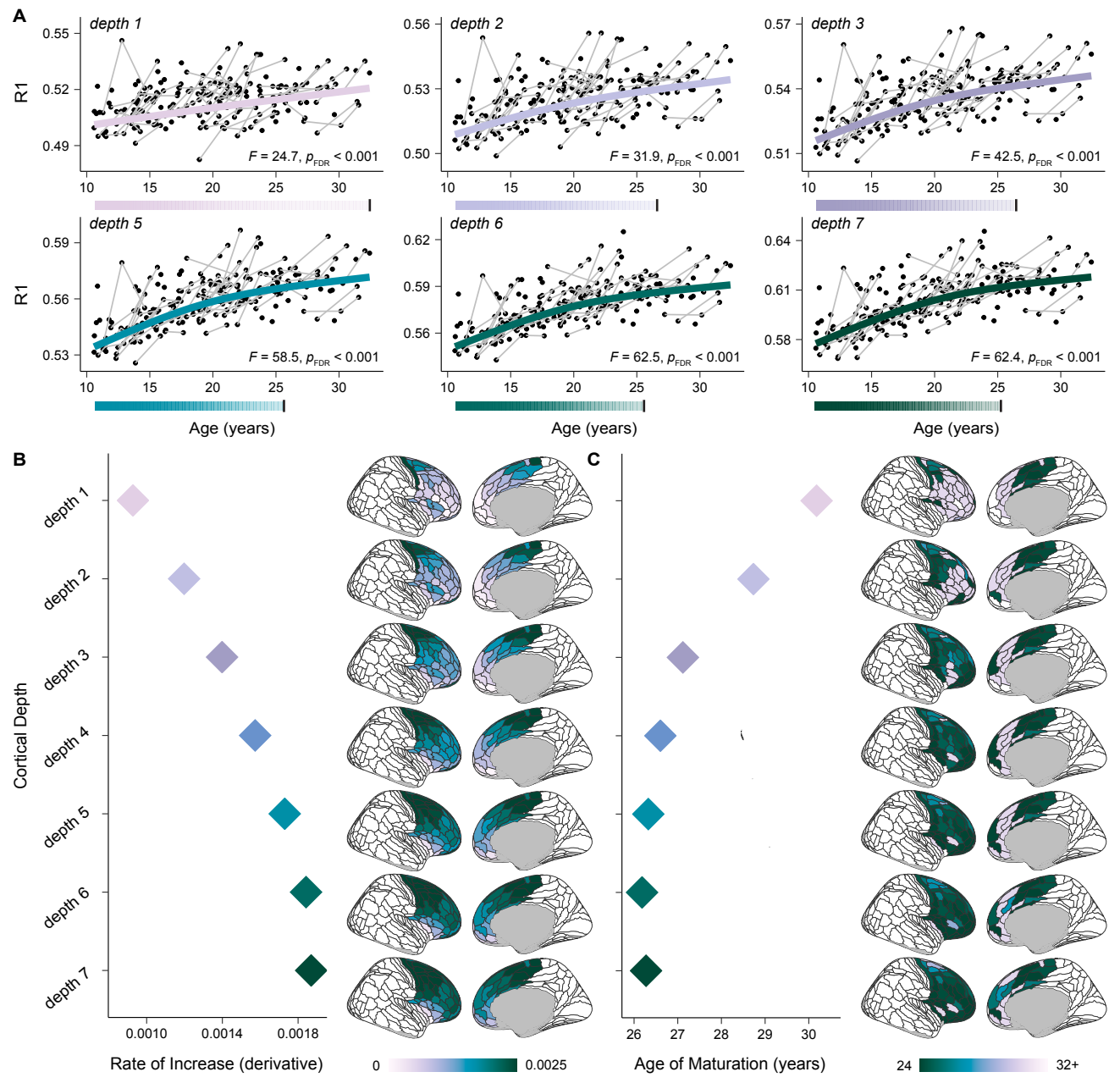
A
depth 1
depth 2
depth 3
depth 5
depth 6
depth 7
R1
F = 24.7, p_FDR < 0.001
F = 31.9, p_FDR < 0.001
F = 42.5, p_FDR < 0.001
F = 58.5, p_FDR < 0.001
F = 62.5, p_FDR < 0.001
F = 62.4, p_FDR < 0.001
Age (years)
B
C
Cortical Depth
Rate of Increase (derivative)
Age of Maturation (years)
0
0.0025
24
32+

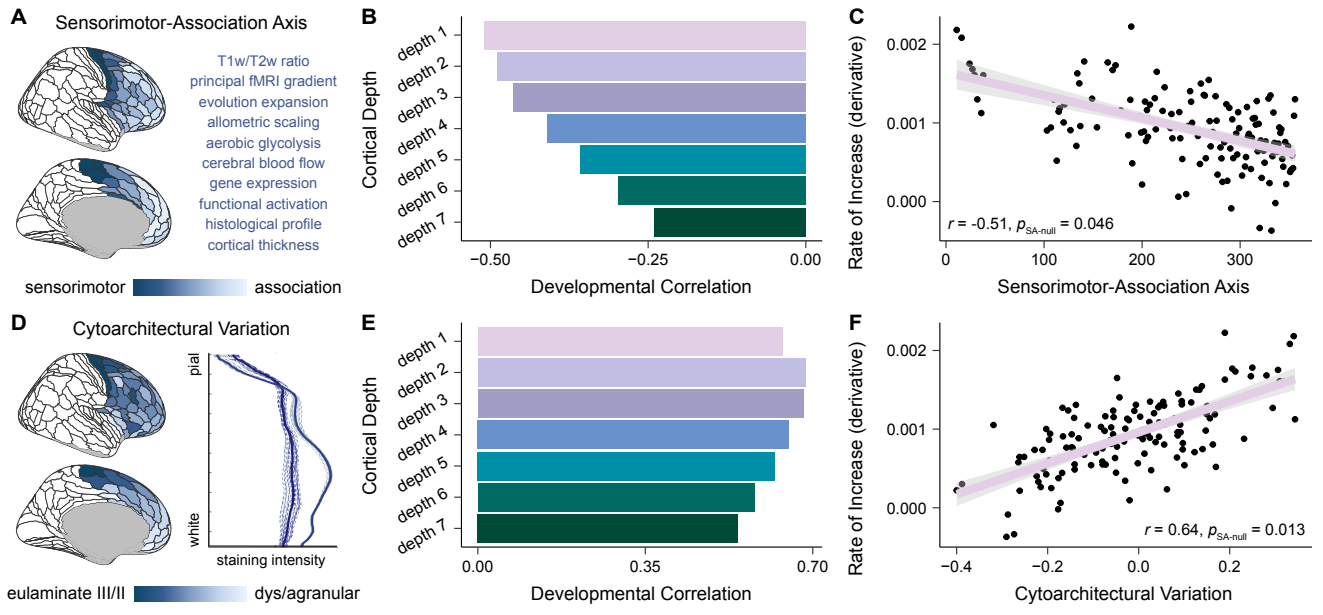
A
Sensorimotor-Association Axis
T1w/T2w ratio
principal fMRI gradient
evolution expansion
allometric scaling
aerobic glycolysis
cerebral blood flow
gene expression
functional activation
histological profile
cortical thickness
sensorimotor
association
B
Cortical Depth
depth 1
depth 2
depth 3
depth 4
depth 5
depth 6
depth 7
−0.50
−0.25
0.00
Developmental Correlation
C
Rate of Increase (derivative)
0.002
0.001
0.000
r = -0.51, p SA-null = 0.046
0
100
200
300
Sensorimotor-Association Axis
D
Cytoarchitectural Variation
pial
white
staining intensity
eulaminate III/II
dys/agranular
E
Cortical Depth
depth 1
depth 2
depth 3
depth 4
depth 5
depth 6
depth 7
0.00
0.35
0.70
Developmental Correlation
F
Rate of Increase (derivative)
0.002
0.001
0.000
r = 0.64, p SA-null = 0.013
−0.4
−0.2
0.0
0.2
Cytoarchitectural Variation

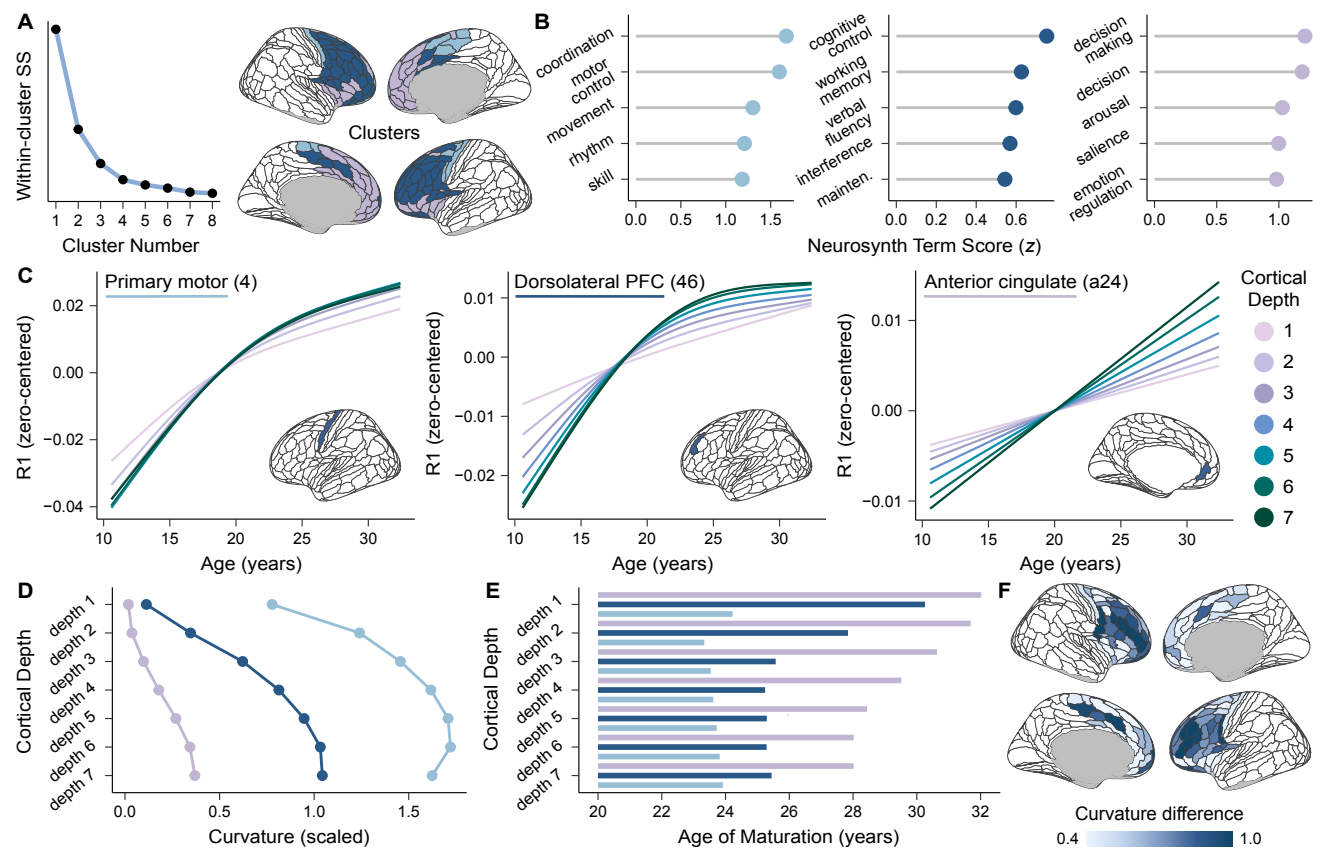
A
Within-cluster SS
1 2 3 4 5 6 7 8
Cluster Number
Clusters
B
coordination
motor control
movement
rhythm
skill
0.0 0.5 1.0 1.5
cognitive control
working memory
verbal fluency
interference
mainten.
0.0 0.2 0.4 0.6
decision making
decision
arousal
salience
emotion regulation
0.0 0.5 1.0
Neurosynth Term Score (z)
C
Primary motor (4)
Dorsolateral PFC (46)
Anterior cingulate (a24)
R1 (zero-centered)
Age (years)
Cortical Depth
1
2
3
4
5
6
7
D
Cortical Depth
depth 1
depth 2
depth 3
depth 4
depth 5
depth 6
depth 7
Curvature (scaled)
E
Age of Maturation (years)
F
Curvature difference
0.4
1.0

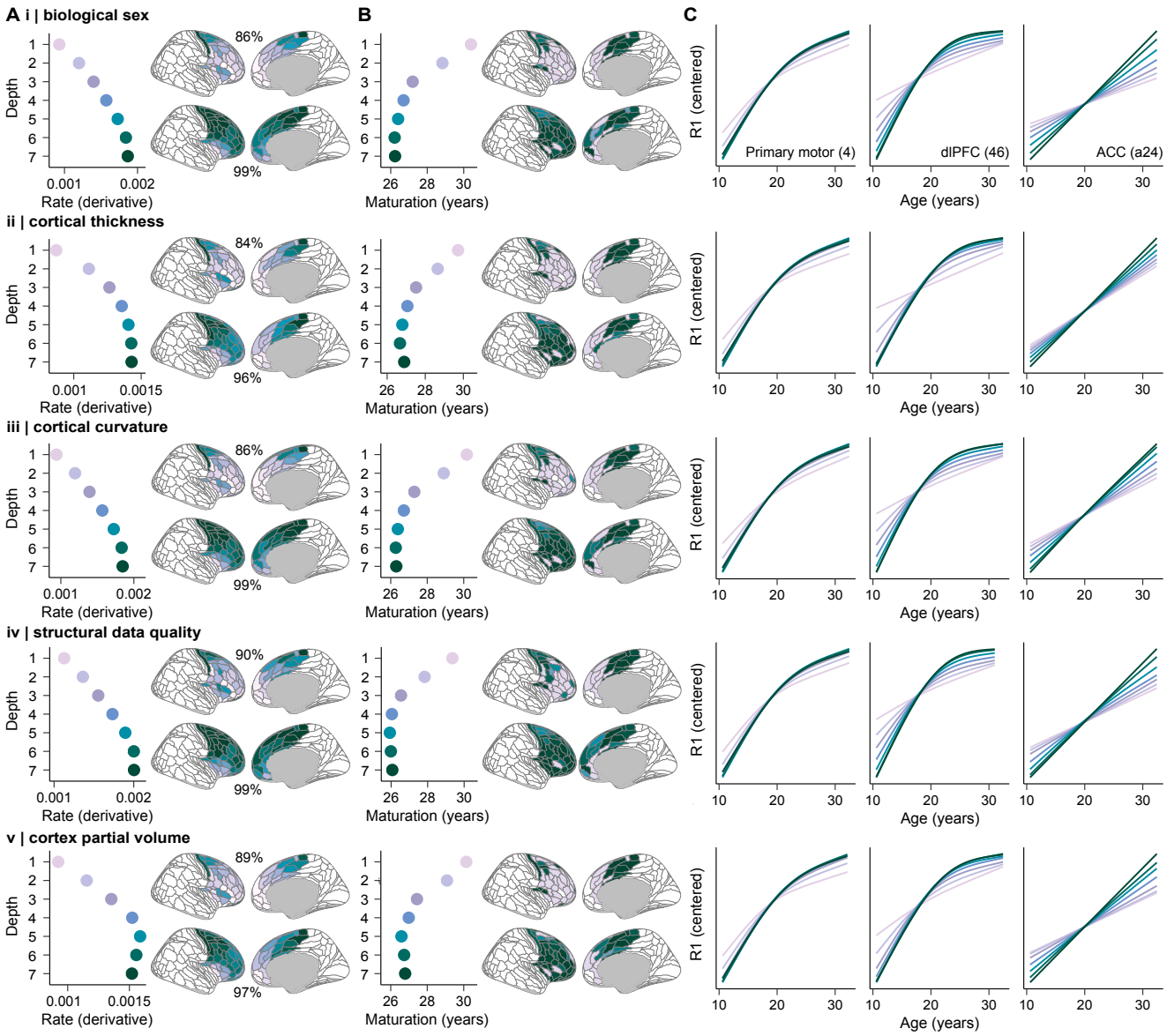
A i | biological sex
ii | cortical thickness
iii | cortical curvature
iv | structural data quality
v | cortex partial volume
B
C
Depth
Rate (derivative)
Maturation (years)
R1 (centered)
Age (years)
Primary motor (4)
dlPFC (46)
ACC (a24)
86%
99%
84%
96%
90%
89%
97%

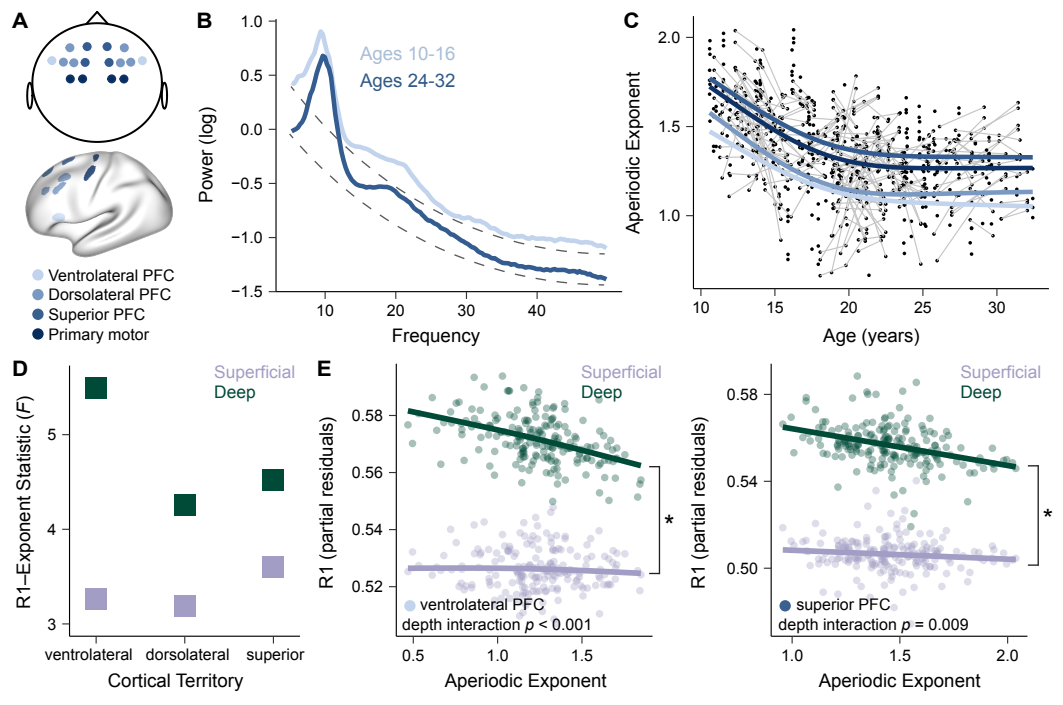
A
Ventrolateral PFC
Dorsolateral PFC
Superior PFC
Primary motor
B
Ages 10-16
Ages 24-32
Power (log)
Frequency
C
Aperiodic Exponent
Age (years)
D
Superficial
Deep
R1–Exponent Statistic (F)
ventrolateral
dorsolateral
superior
Cortical Territory
E
Superficial
Deep
R1 (partial residuals)
ventrolateral PFC
depth interaction p < 0.001
Aperiodic Exponent
superior PFC
depth interaction p = 0.009

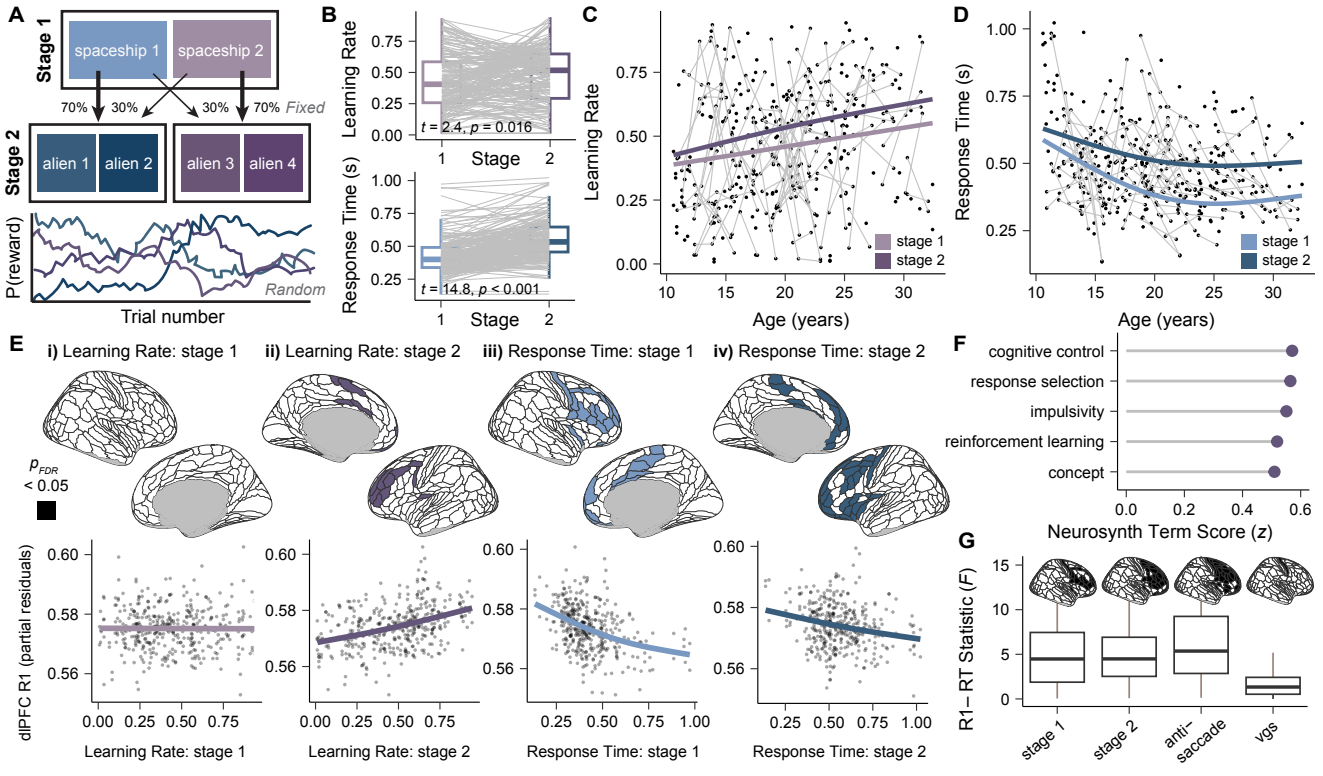
A
Stage 1
spaceship 1
spaceship 2
70%
30%
30%
70%
Fixed
Stage 2
alien 1
alien 2
alien 3
alien 4
P(reward)
Random
Trial number
B
Learning Rate
t = 2.4, p = 0.016
Stage
Response Time (s)
t = 14.8, p < 0.001
Stage
C
Learning Rate
Age (years)
stage 1
stage 2
D
Response Time (s)
Age (years)
stage 1
stage 2
E
i) Learning Rate: stage 1
ii) Learning Rate: stage 2
iii) Response Time: stage 1
iv) Response Time: stage 2
p_FDR < 0.05
dlPFC R1 (partial residuals)
Learning Rate: stage 1
Learning Rate: stage 2
Response Time: stage 1
Response Time: stage 2
F
cognitive control
response selection
impulsivity
reinforcement learning
concept
Neurosynth Term Score (z)
G
R1–RT Statistic (F)
stage 1
stage 2
anti-saccade
vgs